

al

**NASA TECHNICAL
MEMORANDUM**



NASA TM X-2612

NASA TM X-2612

DISTRIBUTION STATEMENT A

Approved for public release;
Distribution Unlimited

**THERMAL PERFORMANCE OF 625-kg/m^3
ELASTOMERIC ABLATIVE MATERIALS ON
SPHERICALLY BLUNTED 0.44-RADIAN CONES**

by Andrew J. Chapman
Langley Research Center
Hampton, Va. 23365

19960418 121

NATIONAL AERONAUTICS AND SPACE ADMINISTRATION • WASHINGTON, D. C. • NOVEMBER 1972

DTIC QUALITY INSPECTED 1

PASTE 17571

DISCLAIMER NOTICE



THIS DOCUMENT IS BEST QUALITY AVAILABLE. THE COPY FURNISHED TO DTIC CONTAINED A SIGNIFICANT NUMBER OF PAGES WHICH DO NOT REPRODUCE LEGIBLY.

1. Report No. NASA TM X-2612	2. Government Accession No.	3. Recipient's Catalog No.	
4. Title and Subtitle THERMAL PERFORMANCE OF 625-kg/m ³ ELASTOMERIC ABLATIVE MATERIALS ON SPHERICALLY BLUNTED 0.44-RADIAN CONES		5. Report Date November 1972	
		6. Performing Organization Code	
7. Author(s) Andrew J. Chapman		8. Performing Organization Report No. L-7974	
		10. Work Unit No. 502-31-50-01	
9. Performing Organization Name and Address NASA Langley Research Center Hampton, Va. 23365		11. Contract or Grant No.	
		13. Type of Report and Period Covered Technical Memorandum	
12. Sponsoring Agency Name and Address National Aeronautics and Space Administration Washington, D.C. 20546		14. Sponsoring Agency Code	
15. Supplementary Notes			
16. Abstract <p>Spherically blunted 0.44-radian (25°) half-angle conical models coated with elastomeric ablative materials were tested in supersonic arc-heated wind tunnels to evaluate performance of the ablators over a range of conditions typical of lifting entry. Four test conditions were combinations of stagnation-point heat-transfer rates of 2.3 and 4.5 MW/m² (200 and 400 Btu/ft²-sec) and stagnation pressures of 20 and 2 kN/m² (0.2 and 0.02 atm). Afterbody values of heat-transfer rate and pressure were 0.05 to 0.20 of stagnation-point values. Stagnation enthalpy varied from 4.4 to 25 MJ/kg (1900 to 11 000 Btu/lbm) and free-stream Mach number was in a range from 3.5 to 4.</p> <p>Ablative materials retained the spherical nose shape throughout tests at the lower heat-transfer level, but receded, assuming a flattened nose shape, during tests at the high heat-transfer level. The residue layer that formed on the conical afterbody was weak, friable, and extensively cracked. The reference ablative material, which contained phenolic microspheres, generally retained the conical shape on the model afterbody. However, a modified ablator, in which phenolic microspheres were replaced with silica microspheres, deformed and separated from the undegraded material, and thereby produced a very uneven surface. Substrate temperatures and ablator recession were in good agreement with values computed by a numerical analysis, for which one set of material properties and environmental data represented the four test conditions.</p>			
17. Key Words (Suggested by Author(s)) Thermal performance of ablators Performance of ablators on cones		18. Distribution Statement Unclassified - Unlimited	
19. Security Classif. (of this report) Unclassified	20. Security Classif. (of this page) Unclassified	21. No. of Pages 52	22. Price* \$3.00

THERMAL PERFORMANCE OF 625-kg/m³ ELASTOMERIC ABLATIVE MATERIALS ON SPHERICALLY BLUNTED 0.44-RADIAN CONES

By Andrew J. Chapman
Langley Research Center

SUMMARY

Spherically blunted 0.44-radian (25°) half-angle conical models coated with elastomeric ablative materials were tested in supersonic arc-heated wind tunnels to evaluate performance of the ablators over a range of conditions typical of lifting entry. Four test conditions were combinations of stagnation-point heat-transfer rates of 2.3 and 4.5 MW/m² (200 and 400 Btu/ft²-sec) and stagnation pressures of 20 and 2 kN/m² (0.2 and 0.02 atm). Afterbody values of heat-transfer rate and pressure were 0.05 to 0.20 of stagnation-point values. Stagnation enthalpy varied from 4.4 to 25 MJ/kg (1900 to 11 000 Btu/lbm) and free-stream Mach number was in a range from 3.5 to 4.

Ablative materials retained the spherical nose shape throughout tests at the lower heat-transfer level, but receded, assuming a flattened nose shape, during tests at the high heat-transfer level. The residue layer that formed on the conical afterbody was weak, friable, and extensively cracked. The reference ablative material, which contained phenolic microspheres, generally retained the conical shape on the model afterbody. However, a modified ablator, in which phenolic microspheres were replaced with silica microspheres, deformed and separated from the undegraded material, and thereby produced a very uneven surface. Substrate temperatures and ablator recession were in good agreement with values computed by a numerical analysis, for which one set of material properties and environmental data represented the four test conditions.

INTRODUCTION

Ablative materials are candidate heat shields for manned lifting entry vehicles such as the space shuttle. However, previous experience with ablative heat shields for manned entry vehicles has been limited primarily to blunt vehicles with low lift-drag ratio, such as Apollo and Gemini. In contrast, lifting entry vehicles, such as the space shuttle, will have slender nose caps and wing leading edges, which, because of the nature of their flow fields, experience a wide variation of pressure and heat-transfer rate between the stagnation region and the afterbody. Such varying conditions may produce residual ablative

layers having markedly different thermal and mechanical properties. This variation in ablator characteristics may affect the compatibility between degraded ablator, undegraded ablator, and structural substrate. Such problems are reported in reference 1, which is an evaluation of ablative materials for use on leading edges of the X-15-2. Requirements for ablative materials on lifting entry vehicles will include – in addition to the earlier criteria of thermal efficiency, integrity, and reliable attachment – a higher order of dimensional stability, compatibility with complex shapes, and limited surface roughness. Consequently, ablators on slender bodies must be tested to evaluate the effects of severe heating gradients on ablator performance.

In the present investigation, ablative materials were tested on 0.44-radian (25°) half-angle conical models having a base radius of 3.8 cm (1.5 in.) and a ratio of nose radius to base radius of 0.2. These models were tested in arc-heated wind tunnels at four test conditions, which were combinations of two levels of heat-transfer rate and two levels of pressure. The test conditions on the model afterbody were in the range of both afterbody and leading-edge conditions predicted for space-shuttle entry. Heating rates at the model stagnation point, although higher than any predicted for the space shuttle, were near the upper limit of ablator usefulness for lifting entry.

The purpose of this investigation was to evaluate systematically the performance of ablators on a slender body at selected conditions representative of lifting entry. This evaluation included characterization of dimensional stability and compatibility with a complex shape, and a comparison of measured ablator performance with calculated results from a numerical analysis. Two elastomeric ablative materials were tested on the conical models. The reference material, identified as E5A1, has been investigated previously as reported in reference 1. The second ablative material was formulated by replacing the phenolic microspheres in the reference material with silica microspheres.

SYMBOLS

Throughout this paper, physical quantities are expressed in the International System of Units (SI). U.S. Customary Units, which are shown in parentheses following the quantities in SI Units, were used for principal measurements and calculations. Conversion factors relating these systems of units are given in appendix A.

H	total enthalpy, J/kg (Btu/lbm)
h	static enthalpy, J/kg (Btu/lbm)
L	arbitrary reference length, m (ft)

N_{Pr}	Prandtl number
p	pressure, N/m^2 (lbf/ft ² , atm)
q	heat-transfer rate, W/m^2 (Btu/ft ² -sec)
R	radius of body spherical nose, m (ft, in.)
r	radius of body of revolution, m (ft, in.)
S	distance along body meridian line measured from forward stagnation point, m (ft, in.)
t	static enthalpy ratio, h_e/H_s
u	velocity component in x-direction, m/sec (ft/sec)
x	chordwise boundary-layer coordinate in physical system, m (ft)
β	pressure-gradient parameter (ref. 2, eq. (25))
γ	isentropic exponent
θ_c	cone semiapex angle, radians (deg)
μ	viscosity, $N\text{-sec}/m^2$ (slugs/ft-sec)
ξ	chordwise boundary-layer coordinate in transformed system
ρ	density, kg/m^3 (slugs/ft ³ , lbm/ft ³)

Subscripts:

c	condition on cone
e	local condition external to boundary layer
o	reference value

s stagnation-point condition

w condition at surface

MODELS AND INSTRUMENTATION

The model shape was a spherically blunted cone having a semiapex angle of 0.44 radian (25°), a ratio of nose radius to base radius of 0.2, and a base radius of 3.8 cm (1.5 in.). Six basic models, having identical exterior shape and dimensions, were tested: a pressure calibration model shown in figure 1(a), a heat-transfer calibration model shown in figure 1(b), two ablative models having an inconel substrate (fig. 2(a)), and two ablative models having an aluminum substrate (fig. 2(b)).

Pressure Model

The pressure model was instrumented with orifices located at the stagnation point and at staggered positions on opposite sides of the model. These locations are described in figure 1(a) by the distance along a meridian line from the stagnation point divided by the nose radius. The pressure model was constructed with a 0.32-cm-thick (0.125-in.) copper wall and was cooled by circulating water so that it could withstand the high-energy stream until pressure measurements stabilized. Orifices were inconel tubing, of 1-mm (0.04-in.) inside diameter, silver soldered in drilled holes and finished flush with the model surface.

Pressures on the model were measured by strain-gage transducers connected to the orifices through the tubing described above and located approximately 3.66 meters (12 ft) from the model. These transducers could sense a pressure range of 0 to 172 kN/m² (0 to 25 psia) and were accurate to within ± 0.43 kN/m² (0.0625 psia). For tests conducted in a very low pressure range, pressures were measured by manometers, in addition to the strain-gage transducers. The manometers were accurate to within approximately ± 0.17 kN/m² (0.025 psia). The manometers were the primary instruments for measuring very low pressures.

Heat-Transfer Model

The thin-wall heat-transfer model, shown in figure 1(b), was a 0.076-cm-thick (0.03-in.) inconel shell. This model was instrumented with 30-gage chromel-alumel thermocouples welded to the inside surface of the shell at the stagnation point and at staggered positions along meridian lines on opposite sides of the model, as shown in figure 1(b). Cold-wall heat-transfer rate on the model at each thermocouple location was determined from thin-skin calorimetry.

Ablative Models

Details of the ablative models are shown in figure 2. The model substrate was a 0.44-radian (25°) truncated cone constructed of either 0.076-cm-thick (0.03-in.) inconel (fig. 2(a)) or 0.15-cm-thick (0.06-in.) aluminum (fig. 2(b)). Thermocouples were attached to the inner surface of the substrate along a meridian line through the model at positions indicated in figure 2. The thin inconel substrate provided a responsive, approximately one-dimensional measure of temperatures at the selected points on the ablator back surface. An aluminum substrate was used in some tests to simulate the heat capacity of a typical aircraft structure. When an ablative coating was applied to the model, the exterior contour was identical to that of the pressure and heat-transfer models. Thickness of the ablative coating on the afterbody was approximately 0.32 cm (0.125 in.).

Composition of the two elastomeric ablative materials is given in table 1. The primary difference between the ablators was the replacement of phenolic microspheres in material I with silica microspheres in material II. These ablators were precast to the shape shown in figure 2 and then bonded to the substrate shell with a low-temperature vulcanizing silicone adhesive.

Five ablative models were tested at each of the four test conditions described in table 2. Three of these models had an inconel substrate, and the remaining two had an aluminum substrate. Two of the inconel-substrate models were covered with material I, and the third inconel model was covered with material II. One aluminum-substrate model was covered with material I, and the second aluminum model was covered with material II.

TESTS

Facilities

Models were tested in two supersonic arc-heated wind tunnels of the Langley entry structures facility. These tunnels are identified as apparatus B and apparatus D.

A diagram of apparatus B is shown in figure 3(a). The test gas is heated in a plenum chamber by a three-phase ac arc. The flow expands through a conical nozzle into an oversize test section and is collected by a diffuser connected to a 3300-m^3 ($117\,000\text{-ft}^3$) vacuum sphere. The vacuum sphere produces a high pressure ratio for overexpanded flow without strong shocks in the test section. Models may be mounted on four hydraulically actuated inserter arms, which are cooled by circulating water and provided with instrumentation connections. Models are stowed away from the test stream during starting and stopping transient conditions and are inserted into the stream after operating conditions stabilize.

Apparatus D has a test section and model installation similar to apparatus B. However, the flow is heated by a dc arc system, which is shown in figure 3(b), and the required pressure ratio is maintained in the test section by a three-stage steam ejector. Apparatus D operates with a lower mass flow rate and produces lower total pressure and higher total enthalpy than apparatus B. A reconstituted air flow is supplied to apparatus D from tanks of oxygen and nitrogen.

Procedure

For each ablative model test, tunnel operation was stabilized at the desired test condition. The test condition was verified by measuring pressure and heat-transfer rate on the appropriate calibration model. The ablative model was then inserted into the test stream for a predetermined exposure time, which produced approximately the same total heat load for all test conditions and which was chosen to allow a significant char layer to develop. Exposure times were 60 seconds for test conditions B-1 and D-1 and 30 seconds for test conditions B-2 and D-2. After exposure was terminated by removing the ablative models from the stream, model substrate temperatures were recorded until maximum temperatures were indicated at each position. A heat-transfer measurement was also made after the ablative test. The heat-transfer rates measured before and after the ablator tests were essentially the same.

RESULTS AND DISCUSSION

Test Conditions

Nominal stream and heating parameter values for each test condition, based on mean values of measured heat-transfer rate and pressure, are listed in table 2. Each stagnation-point heat-transfer rate of approximately 2.3 and 4.5 MW/m² (200 and 400 Btu/ft²-sec) was obtained in both apparatus B and apparatus D. Apparatus B produced a stagnation pressure level of approximately 20 kN/m² (0.2 atm), whereas apparatus D produced a stagnation pressure level of approximately 2 kN/m² (0.02 atm) and higher levels of total enthalpy. These test conditions will subsequently be referred to by the identification used in table 2.

Model stagnation-point heat-transfer rate and stagnation pressure measured during each ablative test are plotted in figure 4. The values for constant stagnation enthalpy were obtained from laminar-flow stagnation-point heat-transfer theory as presented in reference 2. Calculations using this theory are explained in appendix B.

Repeatability of heat-transfer and pressure measurements at test conditions B-1 and B-2, which were obtained in apparatus B, was quite good. Individual values of heat-transfer rate differed from the mean by a maximum of ± 6 percent, and the average

deviation of measured heat-transfer rate from mean values was no more than ± 2 percent. Individual pressure values differed from the mean by as much as ± 4 percent, and average deviation was no more than ± 2 percent.

A much wider deviation of measured heat-transfer rate and pressure values is evident in figure 4 for test conditions D-1 and D-2, which were obtained in apparatus D. Individual values of heat-transfer rate varied as much as ± 18 percent from the mean, whereas the average variation was ± 8 percent from the mean. Individual values of stagnation pressure varied as much as ± 12 percent from the indicated mean value, and the average variation was ± 6 percent from the mean. Flow and pressure were controlled with manual valves and measured with wide-range gages. The low precision of apparatus D is attributed to the resulting inability to accurately control and measure the very low pressure and mass flow rates.

Test-stream properties. - Total-enthalpy values for each test condition shown in table 2 were derived from the theory of reference 2 for the corresponding mean values of the measured stagnation pressure and heat-transfer rate. Free-stream Mach numbers were obtained from the charts of reference 3 by using the derived total-enthalpy values and mean experimental values of model stagnation to total pressure ratio.

Free-stream pressure and enthalpy were obtained from the thermodynamic air charts of reference 4 by an isentropic expansion from stagnation conditions. Corresponding values of free-stream density and viscosity were obtained from the correlation formulas of reference 5 and were used, together with computed free-stream velocity, to compute free-stream Reynolds number and dynamic pressure.

Pressure distribution. - Pressure distributions on the conical model are shown in figure 5. Pressures measured on the model afterbody are divided by the stagnation pressure and are plotted against meridian line distance from the model stagnation point divided by the model nose radius. For test conditions B-1 and B-2, there was only moderate dispersion of the data, most of which fell within the error band of the pressure transducer, which was only 14 percent of the lowest pressures on the model afterbody. An exception is the wide dispersion of the data at the aft-most position on the model.

For test conditions D-1 and D-2, the error band of the transducers far exceeded the very low pressures on the model afterbody, and consequently, only the pressures measured by mercury manometers are shown. Although the lowest pressures on the model afterbody were of the same magnitude as the error band of the manometers, the error range was less than 10 percent of the model stagnation-point pressure. The data are dispersed in alternate directions corresponding to the orifice locations at staggered positions on opposite sides of the model. Consequently, part of the data dispersion may be a result of a slight asymmetry in model alinement.

Theoretical pressure distributions for the spherically blunted conical bodies were calculated from the inviscid-flow-field theory described in reference 6. This theory describes the flow over the entire conical body. The flow is subsonic on the nose near the stagnation point, transonic near the sphere-cone junction, and supersonic on the conical afterbody. Only the data for the supersonic region are shown in figure 5. The theoretical curves show an overexpansion near the sphere-cone junction followed by a recompression farther aft on the cone. Although other experimental data (for example, refs. 7 and 8) have agreed with this theoretical trend, the present data show a continuing expansion on the conical afterbody and differ markedly from the calculations. This difference may be a result of flow from the conical nozzle expanding throughout the test section with a consequent streamwise decrease in free-stream pressure, whereas fully developed flow from a contoured nozzle would possess nearly constant pressure and density in a streamwise direction and would produce a recompression on the conical afterbody similar to that predicted by reference 6 and demonstrated in references 7 and 8.

Heat-transfer-rate distribution. - Heat-transfer-rate distribution on the conical model is shown in figure 6. Each part of this figure represents one of the four test conditions described previously, and each symbol represents heat-transfer rate determined during an ablator test at each condition.

Heat-transfer-rate distributions on the afterbody of a blunted cone were computed by use of the analysis of reference 2 as explained in appendix B. Data required for these computations include stream stagnation properties for each test condition and model pressure distribution. Theoretical heat-transfer-rate distributions, shown in figure 6, were calculated by two methods: by using theoretical pressure distributions and by using experimental pressure distributions, both of which are described in the previous section. Heat-transfer-rate distributions calculated from the experimental pressure distributions, as expected, agree closely with the experimental heat-transfer data. Heat-transfer distributions calculated from the theoretical pressure distributions of reference 6 are only slightly higher than the experimental results. The good agreement between the experimental and theoretical heat-transfer data, regardless of the marked dispersion among the pressure data, illustrates the insensitivity of heat-transfer rate to pressure in this range.

Ablator Morphology

Photographs before test of a typical ablative model coated with material I are shown in figure 7. These photographs show the smooth surface and the contour described in figure 1. Photographs of models after testing at each of the four conditions described in table 2 and figure 4 are shown in figures 8 to 11. Profile, oblique, and front views are shown of each model. All tested models are covered by an extensive system of cracks

to be discussed in detail below. Motion-picture records show that these cracks developed early during exposure in the test stream. Because of the poor mechanical characteristics of the char layers formed, neither of the materials tested is considered suitable for application in environments similar to the test conditions unless some char reinforcement such as honeycomb is provided.

Test condition B-1. - Photographs of a model coated with material I and tested at condition B-1 are shown in figure 8(a). The nose and afterbody generally retained the original contour. However, residual material on the spherical nose was quite different from that over most of the conical afterbody. Higher heating conditions at the nose produced a hard siliceous char, whereas the much lower heating conditions on the afterbody produced a rather friable carbonaceous char. This behavior of elastomeric materials was noted in reference 1. The afterbody surface contained numerous fissures, most of which extended longitudinally from a point just aft of the spherical nose; some of these longitudinal cracks were connected by cracks running in a generally circumferential direction; however, no mechanical removal of the char was observed at any point.

Photographs of a model coated with material II and tested at condition B-1 are shown in figure 8(b). Although the small-radius spherical nose contour was retained, large sections of the charred surface on the afterbody were deformed and separated by very large cracks which revealed undegraded ablator below the charred layer.

Test condition B-2. - Test condition B-2 produced approximately the same pressure as test condition B-1 at approximately twice the heat-transfer-rate level. Photographs of a model coated with material I and tested at condition B-2 are shown in figure 9(a). Heating conditions at the stagnation region flattened the spherical nose and produced a highly siliceous surface layer which showed evidence of molten flow. Examination of photographic records showed that this nose shape was attained early in the 30-second exposure period. The conical shape was maintained on the afterbody with the possible exception of a small deformed area visible in the profile view. The residual char layer on the afterbody was weak and friable like that produced on material I at test condition B-1.

Photographs of a model coated with material II and tested at condition B-2 are shown in figure 9(b). The nose shape is similar to that described for material I at this condition. Material on the conical afterbody, however, experienced widespread cracking and deformation with complete loss of large sections of char layer. A light-colored undegraded area is visible where char was lost during handling after the test. However, the front view shows a large dark area near the nose (1-o'clock position) where the char layer was lost, exposing a lower layer of ablator which had begun to char.

Test condition D-1. - This condition produced approximately the same heat-transfer-rate level as test condition B-1 at approximately one-tenth the pressure level. Photographs of a model coated with material I and tested at condition D-1 are shown in figure 10(a). The surface retained essentially the original contour, including the nose radius, as was the case of test condition B-1. However, the ablative material on the nose region had a carbonaceous appearance like that on the afterbody, rather than the siliceous appearance observed on the nose region after testing at conditions B-1 and B-2. The material on the afterbody was more friable than that on the nose and contained a pattern of cracks which were as numerous but not as large as those formed during test conditions B-1 and B-2.

Photographs of a model coated with material II and tested at condition D-1 are shown in figure 10(b). Although material II retained the spherical nose radius at this condition, the contour on the afterbody was distorted by deformed areas of char separated by large cracks.

Test condition D-2. - This test condition produced the higher heat-transfer-rate level corresponding to condition B-2 and the lower pressure level corresponding to condition D-1. Photographs of a model coated with material I and tested at condition D-2 are shown in figure 11(a). Appearance of the material on the afterbody was much like that at test condition D-1. However, the spherical nose ablated to a concave shape, and the residual material in this concave nose region had the glassy appearance observed at test condition B-2.

Photographs of a model coated with material II and tested at condition D-2 are shown in figure 11(b). The concave nose region noted for material I at this condition was also produced on material II. Large cracks formed on the afterbody, and sections of charred material deformed and separated from the lower undegraded ablator.

Ablator recession. - Models coated with material I and tested at each of the four test conditions were sectioned in order to measure the thickness of the degraded and undegraded layers. Photographs of these sections are shown in figure 12. Before the models were sectioned, the surface was coated with a thin layer of clear epoxy to protect the char layer. Models coated with material II were not sectioned because the deformed condition of much of the char precluded meaningful char-layer thickness measurements. The section photographs in figure 12 show, at all test conditions, a zone of partial separation between the char layer and the undegraded layer.

Char-layer and undegraded-layer thicknesses at various positions on the model surface are shown for material I in figure 13. At the stagnation point the greatest char-layer recession occurred at test conditions B-2 and D-2, whereas on the afterbody, the

degraded layers showed the characteristic tendencies of elastomeric resins to expand at low heating rates.

Comparison of Experimental and Calculated Ablator Performance

Ablative-material temperatures and recession have been calculated for the four test conditions by use of the numerical analysis described in reference 9. Inputs to this program include environmental conditions such as heat-transfer rate, enthalpy, and heat-transfer-rate distribution. The program also requires a set of thermophysical properties such as those listed in table 3.

Because a complete set of property data was not available, certain properties were inferred in order to obtain a complete set which would represent the experimental results. The properties listed in table 3(a) for the unpyrolyzed ablator are measured data for material I. Properties for pyrolysis products and the char layer are based on possible chemical compositions of the reaction products. For example, specific-heat values of the pyrolysis gases are those for CH_4 , and thermal conductivity for the char was obtained by varying slightly the values for SiO_2 . The kinetic parameters for ablator pyrolysis – the reaction-rate constant and the activation-energy constant – were initially based on experimental data and were iterated to match the computed char-uncharred material interface with thickness measured after the tests. Matching the interface positions in this way was also one of the more forceful variations for matching the computed and measured substrate temperatures. An iterative procedure such as this was used in reference 10 to match property data to one set of test conditions, whereas in the present investigation, one set of property data is matched to four test conditions. Such an inductive process, if carried out over a wide enough range of conditions, should produce a set of property data which characterizes the ablative performance of the material within the applicable range. In view of the different ablator reactions at various environmental conditions, such property data should be used only within the range of conditions for which it was produced. For example, the present set of ablator properties should be used only for afterbody heating conditions within the range reported herein unless it can be shown that they are valid for other conditions.

Experimental and computed ablator responses at $\frac{S}{R} = 5$ on the inconel-substrate models are compared in figure 14. The analysis computed surface recession only as a function of surface temperature and oxidation. However, in the present tests, the silica content of the residual layer on the afterbody prevented oxidation and recession. Although there is no mechanism in the analysis to predict char expansion, such expansion is characteristic of elastomeric ablators and was observed in tests at all conditions. Computed interface recessions were in close agreement with measured interface recessions at the end of tests. The interface position was taken as the separation plane shown in figure 12.

Computed values of substrate temperatures were in close agreement with measured values at each test condition.

Experimental and computed ablator responses at $\frac{S}{R} = 4$ on the aluminum-substrate models are compared in figure 15. Inputs for these calculations were identical to those used for models with an inconel substrate, except for the slightly greater heat capacity of the aluminum substrate and a more forward thermocouple position on the model afterbody. A comparison of these two sets of calculations shows that, at corresponding test conditions, the temperature of the aluminum substrate, because of the higher heat capacity of the aluminum, was lower than the temperature of the inconel substrate. However, measured temperatures on aluminum substrates were, at all test conditions, lower than computed temperatures. In view of the good agreement between measured and computed temperatures on the inconel substrate, differences between measured and computed temperatures on the aluminum substrates may be due to the much stronger effect of two-dimensional conduction through the thicker, higher conductivity aluminum.

The temperature histories measured at $\frac{S}{R} = 5$ and $\frac{S}{R} = 4$ on the inconel and aluminum substrates are similar to the temperature histories measured at all other points on the afterbody. These temperature histories can be characterized by the temperature at several times during exposure and the maximum temperature which occurred after termination of exposure. In figure 16 substrate temperature is shown as a function of position on the model afterbody. These temperature distributions are shown for 30 seconds (the exposure period for test conditions B-2 and D-2), 60 seconds (the exposure period for test conditions B-1 and D-1), and maximum temperature.

Computed temperature distributions are compared in figure 16(a) with temperature distributions measured on inconel-substrate models coated with material I. Computed temperatures are in fair agreement with measured temperatures for shorter exposure times, especially test conditions B-2 and D-2, but tend to be higher than temperatures for 60-second exposure and maximum temperatures for test conditions B-1 and D-1. This agreement for material I on inconel is such that the analysis should be adequate for predicting heat-shield requirements at all points on the model afterbody.

Temperatures measured on inconel substrates covered with material II (fig. 16(b)) were somewhat higher than those on inconel substrates coated with material I and were more uneven in keeping with the more uneven residual surfaces on material II. Computed temperatures were slightly lower than measured temperatures over most of the body.

Temperatures measured on the aluminum-substrate models (figs. 16(c) and (d)) showed little variation between model positions. This nearly uniform temperature distribution is due to multidimensional conduction through the relatively thick, high-conductivity aluminum shell, which permitted temperatures to equalize quickly even

though heating rates varied from point to point. Since the analysis does not account for such multidimensional effects, computed temperatures were much higher than measured temperatures on the aluminum substrate.

CONCLUDING REMARKS

Spherically blunted 0.44-radian (25°) half-angle conical models coated with ablative heat-shield materials were tested in supersonic arc-heated wind tunnels. The reference ablative material was a silicone resin filled with phenolic and silica microspheres and silica fibers. The second ablative material contained the same silicone resin and fillers except that the phenolic microspheres were replaced with an equal mass of silica microspheres. Both ablators had a density of approximately 625 kg/m^3 (39 lbm/ft^3).

The conical models were tested at four conditions which were combinations of two levels of stagnation-point heat-transfer rate, approximately 2.3 and 4.5 MW/m^2 (200 and $400 \text{ Btu/ft}^2\text{-sec}$), and two levels of stagnation pressure, approximately 20 and 2 kN/m^2 (0.2 and 0.02 atm). Afterbody values of heat-transfer rate and pressure were 0.05 to 0.20 of stagnation-point values. Stagnation enthalpy varied from 4.4 to 25 MJ/kg (1900 to $11\,000 \text{ Btu/lbm}$). The Mach number range for the tests was 3.5 to 4 , and the free-stream Reynolds number was 3000 per meter (900 per foot) for the highest enthalpy test condition and $200\,000$ per meter ($62\,000$ per foot) for the lowest enthalpy test condition.

Neither of the materials tested proved suitable for application in the heating environments used in this program. Both materials produced weak, friable char layers on the conical afterbody. The char layer that formed from the reference elastomeric ablative material developed large cracks but generally retained the conical shape on the model afterbody. However, the char layer formed from the modified elastomer, in which silica microspheres replaced the phenolic microspheres, produced a very uneven surface because the char separated from the undegraded material. Those results show that the materials tested require char reinforcement, such as honeycomb, before they can be considered for application in environments similar to the ones used in the tests.

Ablator performance was compared with results from a numerical analysis for charring ablators. One set of ablator property data was used for all calculations, and environmental data were varied to represent the four tunnel conditions of the tests. For the reference elastomeric material, the computed recession agreed well with the observed recession of the char-undegraded material interface. Computed substrate temperatures agreed closely with temperatures measured on inconel-substrate models but were higher than temperatures measured on aluminum-substrate models. Within the range of test conditions, the performance of the reference ablator was predictable, regardless of the irregular surface conditions.

Pressure and heat-transfer distributions were measured at the four test conditions on suitably instrumented models having the same configuration as the ablative models described above. Measured afterbody pressures had a rather wide band of dispersion due to insensitivity of the gages to the very low pressures. Pressures calculated from an inviscid-flow theory were somewhat higher than the inconsistent measured pressures.

Measured heat-transfer distributions were only moderately scattered among runs at each test condition, and a theoretical heat-transfer distribution based on locally similar solutions to boundary-layer equations agreed well with experimental results when an average of the experimental pressure distributions was used in the calculations. When pressures predicted by the inviscid-flow theory were used in the calculations, the theoretical heat-transfer distributions were only moderately higher than the experimental results.

Langley Research Center,
National Aeronautics and Space Administration,
Hampton, Va., August 28, 1972.

APPENDIX A

CONVERSION OF SI UNITS TO U.S. CUSTOMARY UNITS

Conversion factors required for units used herein are given in the following table:

Physical quantity	SI Unit	Conversion factor	U.S. Customary Unit
Density	kilograms/meter ³ (kg/m ³)	$\begin{cases} 1.94 \times 10^{-3} \\ 62.43 \times 10^{-3} \end{cases}$	$\begin{cases} \text{slugs/ft}^3 \\ \text{lbm/ft}^3 \end{cases}$
Enthalpy	joules/kilogram (J/kg)	430.21×10^{-6}	Btu/lbm
Heat-transfer rate	watts/meter ² (W/m ²)	88.114×10^{-6}	Btu/ft ² -sec
Length	meters (m)	$\begin{cases} 3.28 \\ 39.37 \end{cases}$	$\begin{cases} \text{ft} \\ \text{in.} \end{cases}$
Pressure	newtons/meter ² (N/m ²)	$\begin{cases} 20.89 \times 10^{-3} \\ 9.869 \times 10^{-6} \end{cases}$	$\begin{cases} \text{lbf/ft}^2 \\ \text{atm} \end{cases}$
Specific heat	joules/kilogram-K (J/kg-K)	0.239×10^{-3}	Btu/lbm-°R
Specific reaction rate	kilograms/meter ² -second (kg/m ² -sec)	0.205	lbm/ft ² -sec
Temperature	kelvin (K)	1.8	°R
Thermal conductivity	watts/meter-kelvin (W/m-K)	0.16×10^{-3}	Btu/ft-sec-°R
Velocity	meters/second	3.28	ft/sec
Viscosity	newton-seconds/meter ² (N-sec/m ²)	0.021	slugs/ft-sec

Prefixes to indicate multiples of units are as follows:

Prefix	Multiple
mega (M)	10 ⁶
kilo (k)	10 ³
centi (c)	10 ⁻²
milli (m)	10 ⁻³

APPENDIX B

HEAT-TRANSFER CALCULATIONS

The analysis of reference 2 was used to calculate laminar convective heat-transfer rate to the surface of the spherically tipped cone.

Stagnation enthalpy was calculated from equation (39) of reference 2,

$$-q_{w,s} = 0.767(\rho_w \mu_w)_s^{0.07} (\rho_e \mu_e)_s^{0.43} (H_e - h_w)_s (N_{Pr,w,s})^{-0.6} \left(\frac{du_e}{dx} \right)_s^{0.5} \quad (B1)$$

The Newtonian flow relation was used for the stagnation-point velocity gradient

$$\left(\frac{du_e}{dx} \right)_s = \left(\frac{2p_s}{\rho_s} \right)^{0.5} \frac{1}{R}$$

Equation (B1) was evaluated for a range of stagnation enthalpy H_s and stagnation pressure p_s encompassing the conditions of the present tests. Values for density ρ and the density-viscosity product $\rho\mu$ were computed from the correlating formulas of reference 5. Results from the evaluation of equation (B1) are shown in figure 4.

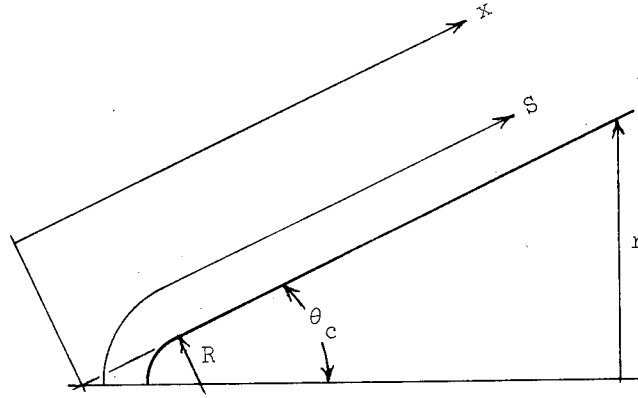
Heat-transfer distribution on a blunt body of revolution is given in reference 2 (eq. (63)) as

$$\frac{q_w}{q_{w,s}} = \frac{\left(\frac{\rho_w \mu_w u_e r}{\mu_o L \sqrt{2\xi}} \right)_c}{\left[2\rho_w \mu_w \left(\frac{du_e}{dx} \right)_s \right]^{0.5}} \left[1.033 \left(\frac{1 + 0.527\beta^{0.686}}{1.116 + 0.411\beta^{0.686}} \right) (0.85 + 0.15t_e) (1.1 - 0.1625t_e - 0.0625t_e^2) \right] \quad (B2)$$

where ξ is a transformed coordinate parallel to the body surface, β is a pressure gradient parameter, t_e is a dimensionless static enthalpy, and L a characteristic body dimension.

The coordinate system applicable to the blunted cone is shown in the following sketch:

APPENDIX B - Continued



Sketch (a)

From sketch (a) it may be seen that the chordwise coordinates on a sharp cone and on a spherically blunted cone have the following relation:

$$\frac{x}{R} = \cot \theta_c + \frac{S}{R} - \frac{\pi}{2} + \theta_c \quad (B3)$$

The transformed coordinate along the body surface is defined in reference 2 as

$$\xi = \frac{1}{2} \int_0^x \frac{\rho_w \mu_w u_e}{\mu_o} \left(\frac{r}{L} \right)^2 dx \quad (B4a)$$

By using the relations between coordinates shown in sketch (a)

$$\xi = \frac{1}{2} \int_0^x \frac{\rho_w \mu_w u_e}{\mu_o} \frac{\sin^2 \theta_c}{L^2} x^2 dx \quad (B4b)$$

In conical flow all variables are independent of x or ξ so that

$$\xi = \frac{1}{2} \left(\frac{\rho_w \mu_w}{\mu_o} \right)_c u_e \frac{\sin^2 \theta_c}{L^2} \frac{x^3}{3} \quad (B4c)$$

and, from reference 2, equation (25), $\beta = 0$ since $\frac{du_e}{dx} = 0$ on the conical surface.

By combining equations (B2), (B3), and (B4), the heat-transfer distribution on the conical surface may be written as

$$\frac{q_c}{q_s} = \frac{\sqrt{3}}{2} \left[\frac{(\rho_w \mu_w)_c}{(\rho_w \mu_w)_s} \right]^{0.5} \left[\frac{u_{e,c}}{\left(\frac{du_e}{dx} \right)_s} \right]^{0.5} \left[R \cot \theta_c + S - R \left(\frac{\pi}{2} - \theta_c \right) \right]^{-0.5} \left[0.926(0.85 + 0.15t_e)(1.1 - 0.1625t_e + 0.0625t_e^2) \right] \quad (B5)$$

APPENDIX B – Concluded

The following perfect-gas isentropic-flow relations have been used to evaluate equation (B2):

$$u_{e,c} = \left\{ 2H_s \left[1 - \left(\frac{p_c}{p_s} \right)^{\frac{\gamma-1}{\gamma}} \right] \right\}^{0.5}$$

$$\left(\frac{du_e}{dx} \right)_s = \frac{1}{R} \left(\frac{2p_s}{\rho_s} \right)^{0.5}$$

$$t_e = \frac{h_e}{H_s} = \left(\frac{p_c}{p_s} \right)^{\frac{\gamma-1}{\gamma}}$$

Also, the following relation from reference 5 was used

$$\frac{(\rho_w^{\mu_w})_c}{(\rho_w^{\mu_w})_s} = \left(\frac{p_c}{p_s} \right)^{0.992}$$

Heat-transfer distribution on a spherically blunted cone in a perfect-gas flow expanding isentropically from the stagnation point may be expressed in the following manner:

$$\frac{q_c}{q_s} = \frac{0.866 \left[\frac{(\rho_w^{\mu_w})_c}{(\rho_w^{\mu_w})_s} \right]^{0.5} \left\{ \left[1 - \left(\frac{p_c}{p_s} \right)^{\frac{\gamma-1}{\gamma}} \right] \frac{\rho_s}{p_s} H_s \right\}^{0.25}}{\left(\frac{S}{R} + \cot \theta_c - \theta_c - \frac{\pi}{2} \right)^{0.5}} \left\{ 0.926 \left[0.85 + 0.15 \left(\frac{p_c}{p_s} \right)^{\frac{\gamma-1}{\gamma}} \right] \left[1.1 - 0.1625 \left(\frac{p_c}{p_s} \right)^{\frac{\gamma-1}{\gamma}} + 0.0625 \left(\frac{p_c}{p_s} \right)^{2 \left(\frac{\gamma-1}{\gamma} \right)} \right] \right\} \quad (B6)$$

Heat-transfer distribution has been evaluated from equation (B6) for the four test conditions reported herein by using experimental values of pressure distribution p_c/p_s and theoretical values of p_c/p_s obtained from the inviscid-flow-field theory of reference 6. Results of these calculations together with experimental data are shown in figure 6.

REFERENCES

1. Chapman, Andrew J.; and Dow, Marvin B.: Arc-Tunnel Evaluation of Some Ablative Heat Shield Materials for the X-15-2. NASA TN D-3753, 1967.
2. Cohen, Nathaniel B.: Boundary-Layer Similar Solutions and Correlation Equations for Laminar Heat-Transfer Distribution in Equilibrium Air at Velocities up to 41,000 Feet Per Second. NASA TR R-118, 1961.
3. Jorgensen, Leland H.; and Baum, Gayle M.: Charts for Equilibrium Flow Properties of Air in Hypervelocity Nozzles. NASA TN D-1333, 1962.
4. Moeckel, W. E.; and Weston, Kenneth C.: Composition and Thermodynamic Properties of Air in Chemical Equilibrium. NACA TN 4265, 1958.
5. Cohen, Nathaniel B.: Correlation Formulas and Tables of Density and Some Transport Properties of Equilibrium Dissociating Air For Use in Solutions of the Boundary-Layer Equations. NASA TN D-194, 1960.
6. Inouye, Mamoru; Rakich, John V.; and Lomax, Harvard: A Description of Numerical Methods and Computer Programs for Two-Dimensional and Axisymmetric Supersonic Flow Over Blunt-Nosed and Flared Bodies. NASA TN D-2970, 1965.
7. Creel, Theodore, R., Jr.; Miller, Charles G., III; Maddalon, Dal V.; and Watson, Ralph D.: Pressure Distributions and Aerodynamic Characteristics of 9° and 15° Blunted Cones in Nitrogen and Helium at Mach 20. NASA TN D-4314, 1968.
8. Wagner, Richard D., Jr.; and Watson, Ralph: Induced Pressures and Shock Shapes on Blunt Cones in Hypersonic Flow. NASA TN D-2182, 1964.
9. Swann, Robert T.; Pittman, Claud M.; and Smith, James C.: One-Dimensional Numerical Analysis of the Transient Response of Thermal Protection Systems. NASA TN D-2976, 1965.
10. Pittman, Claud M.; and Brewer, William D.: Analytical Determination of the Effect of Thermal Property Variations on the Performance of a Charring Ablator. NASA TN D-3486, 1966.

TABLE 1.- COMPOSITION OF ABLATIVE MATERIALS

Component	Percent by mass of ablative material -	
	I (E5A1)	II
Silicone resin ^a (General Electric RTV-602)	70	70
Hollow silica spheres	10	19
Silica fibers	4	4
Hollow phenolic spheres	9	0
Silicone fluid (General Electric SF-69)	3.5	3.5
Silicone primer (General Electric SS-4004)	3.5	3.5

^a Percent mass of silicone resin includes 0.5 percent catalyst (General Electric SRC-04).

TABLE 2.- NOMINAL TEST CONDITIONS

(a) SI Units

Test condition	Tunnel B		Tunnel D	
	B-1	B-2	D-1	D-2
Total enthalpy, H , MJ/kg	4.4	8.4	14.0	25.6
Total pressure, ^a p_s , kN/m ²	274.0	269.0	24.0	20.0
Free-stream Mach number	4.1	3.6	3.9	3.5
Free-stream Reynolds number per meter	203 000	108 000	5200	3000
Free-stream dynamic pressure, kN/m ²	10.6	11.0	0.8	0.8
Stagnation pressure on model, ^a p_s , kN/m ²	19.8	18.8	2.0	2.3
Stagnation-point heat-transfer rate, ^a $q_{w,s}$, MW/m ²	2.2	4.4	2.4	4.8
Stream composition	Air		Reconstituted air	
Nozzle exit diameter, mm	152		102	

(b) U.S. Customary Units

Test condition	Tunnel B		Tunnel D	
	B-1	B-2	D-1	D-2
Total enthalpy, H , Btu/lbm	1900	3600	6000	11 000
Total pressure, ^a atm	2.70	2.65	0.24	0.20
Free-stream Mach number	4.1	3.6	3.9	3.5
Free-stream Reynolds number per foot	62 000	33 000	1600	900
Free-stream dynamic pressure, lbf/ft ²	220	230	17	17
Stagnation pressure on model, ^a p_s , atm	0.195	0.185	0.020	0.022
Stagnation-point heat-transfer rate, ^a $q_{w,s}$, Btu/ft ² -sec	195	390	210	420
Stream composition	Air		Reconstituted air	
Nozzle exit diameter, in.	6		4	

^a Measured values.

TABLE 3.- MODEL ABLATOR PROPERTIES USED IN
ABLATION ANALYSIS

(a) Properties of unpyrolyzed ablator

Temperature		Thermal conductivity		Specific heat	
K	°R	W/m-K	Btu/ft-sec-°R	kJ/kg-K	Btu/lb-°R
278	500	0.094	1.5×10^{-5}	1.48	0.354
311	560	↓	↓	1.53	.365
367	660			1.60	.382
422	760			1.66	.396
478	860			1.72	.41
533	960			1.75	.419
589	1060			1.79	.427
644	1160			↓	↓
Density, kg/m ³ (lbm/ft ³) 625 (39)					

TABLE 3.- MODEL ABLATOR PROPERTIES USED IN
ABLATION ANALYSIS - Continued

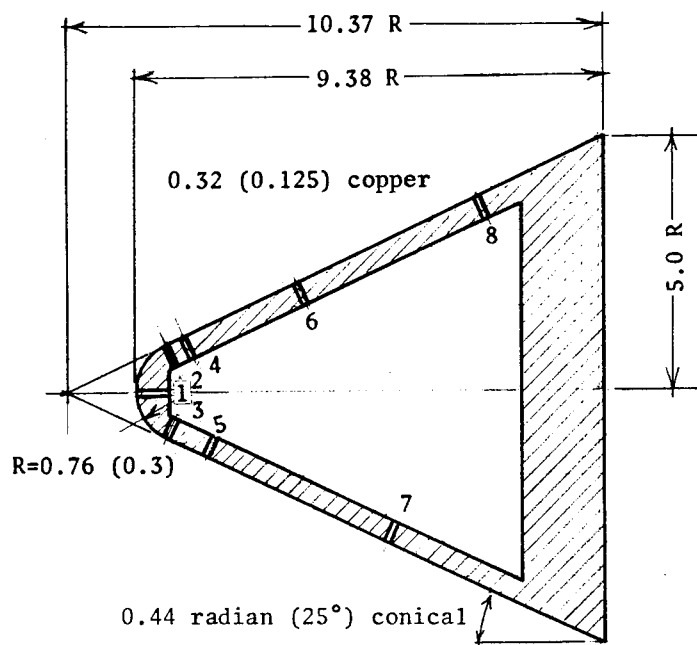
(b) Pyrolysis characteristics and properties of pyrolysis products

Temperature		Specific heat of pyrolysis gases	
K	°R	kJ/kg-K	Btu/lb-°R
300	540	2.22	0.53
556	1000	3.10	.74
694	1250	3.56	.85
833	1500	4.02	.96
1000	1800	4.48	1.07
1111	2000	4.73	1.13
1250	2250	4.98	1.19
1389	2500	5.23	1.25
1528	2750	5.44	1.3
1667	3000	5.61	1.34
1944	3500	5.86	1.4
2222	4000	5.98	1.43
Effective heat of pyrolysis, kJ/kg (Btu/lbm) 465 (200)			
Specific reaction rate constant for pyrolysis of			
original ablator, Mg/m ² -sec (lbm/ft ² -sec) 12 (2.5 × 10 ³)			
Activation energy constant for pyrolysis of			
original ablator, K (°R) 13 300 (24 000)			

TABLE 3.- MODEL ABLATOR PROPERTIES USED IN
ABLATION ANALYSIS – Concluded

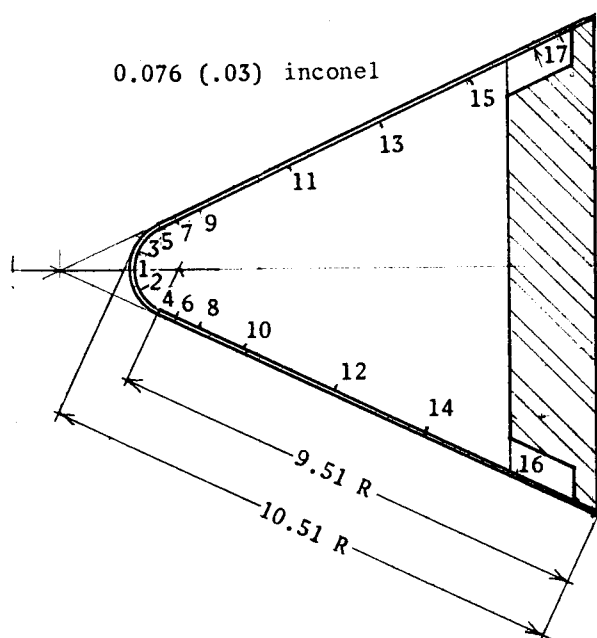
(c) Charred ablator properties

Temperature		Thermal conductivity		Specific heat	
K	°R	W/m-K	Btu/ft-sec-°R	kJ/kg-K	Btu/lbm-°R
278	500	0.12	1.9×10^{-5}	0.96	0.23
556	1000	.15	2.4	1.26	.3
833	1500	.18	2.9	1.46	.35
1110	2000	.21	3.3	1.55	.37
1390	2500	.23	3.7	1.59	.38
1667	3000	.25	4.0	1.51	.39
1944	3500	.26	4.2	1.67	.40
2220	4000	.28	4.4	1.72	.41
Density, kg/m ³ (lbm/ft ³) 137 (8.6)					
Heat of sublimation, kJ/kg (Btu/lbm) 139 (60)					
Emissivity 0.8					
Specific reaction-rate constant for char removal,					
Mg/m ² -sec-atm ^{1/2} (lbm/ft ² -sec-atm ^{1/2}) 4.9×10^7 (1×10^{10})					
Activation-energy constant, K (°R) 425 000 (765 000)					



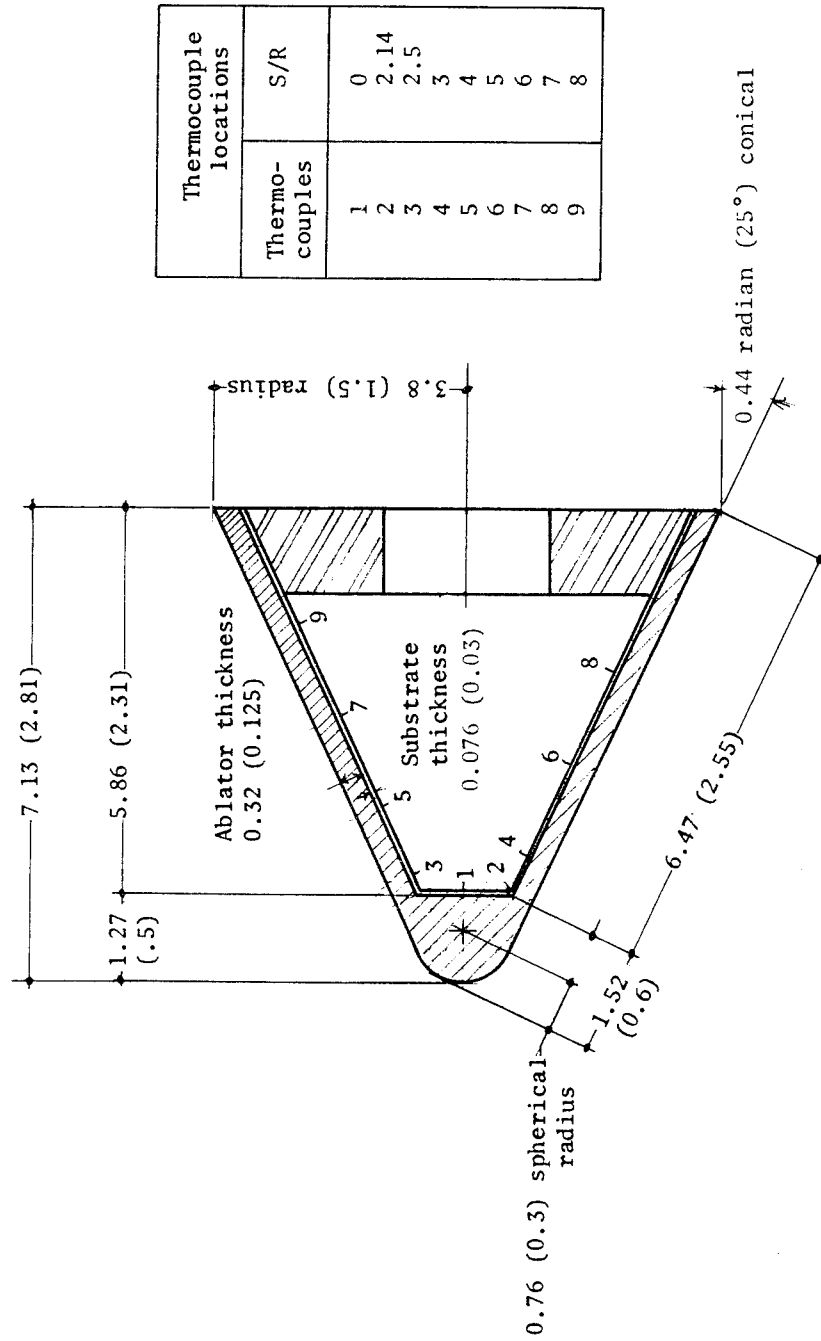
(a) Pressure model.

Pressure orifice location	Thermocouple position	S/R
1	1	0
	2	.44
	3	.44
2	4	1.13
3	5	1.13
	6	1.5
4	7	1.5
5	8	2.
	9	2.
	10	3.
6	11	4.
	12	5.
7	13	6.
	14	7.
8	15	8.
	16	9.
	17	10.



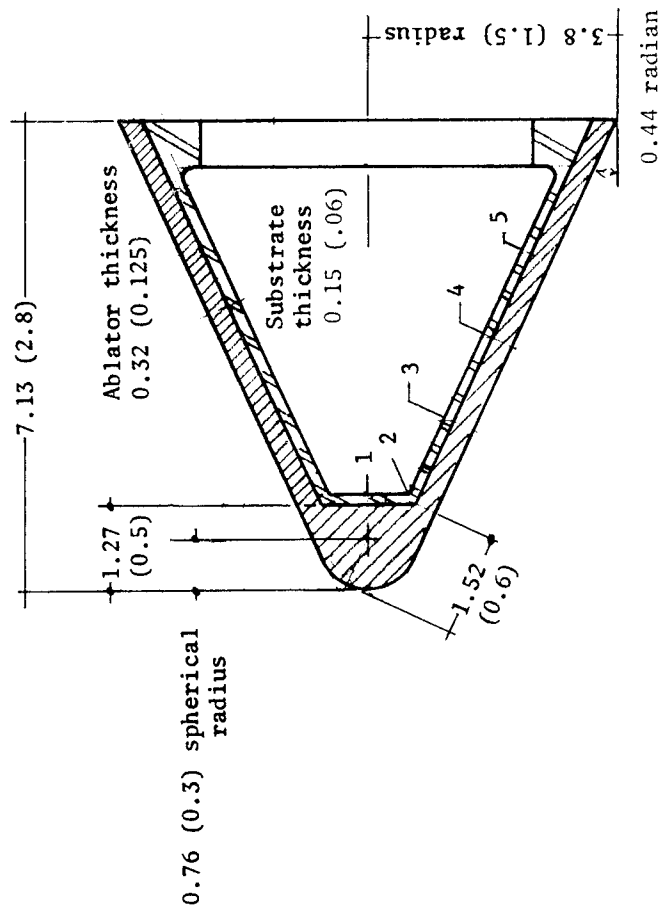
(b) Heat-transfer model.

Figure 1.- Configuration of calibration models. Linear dimensions are in centimeters (inches).



(a) Inconel substrate.

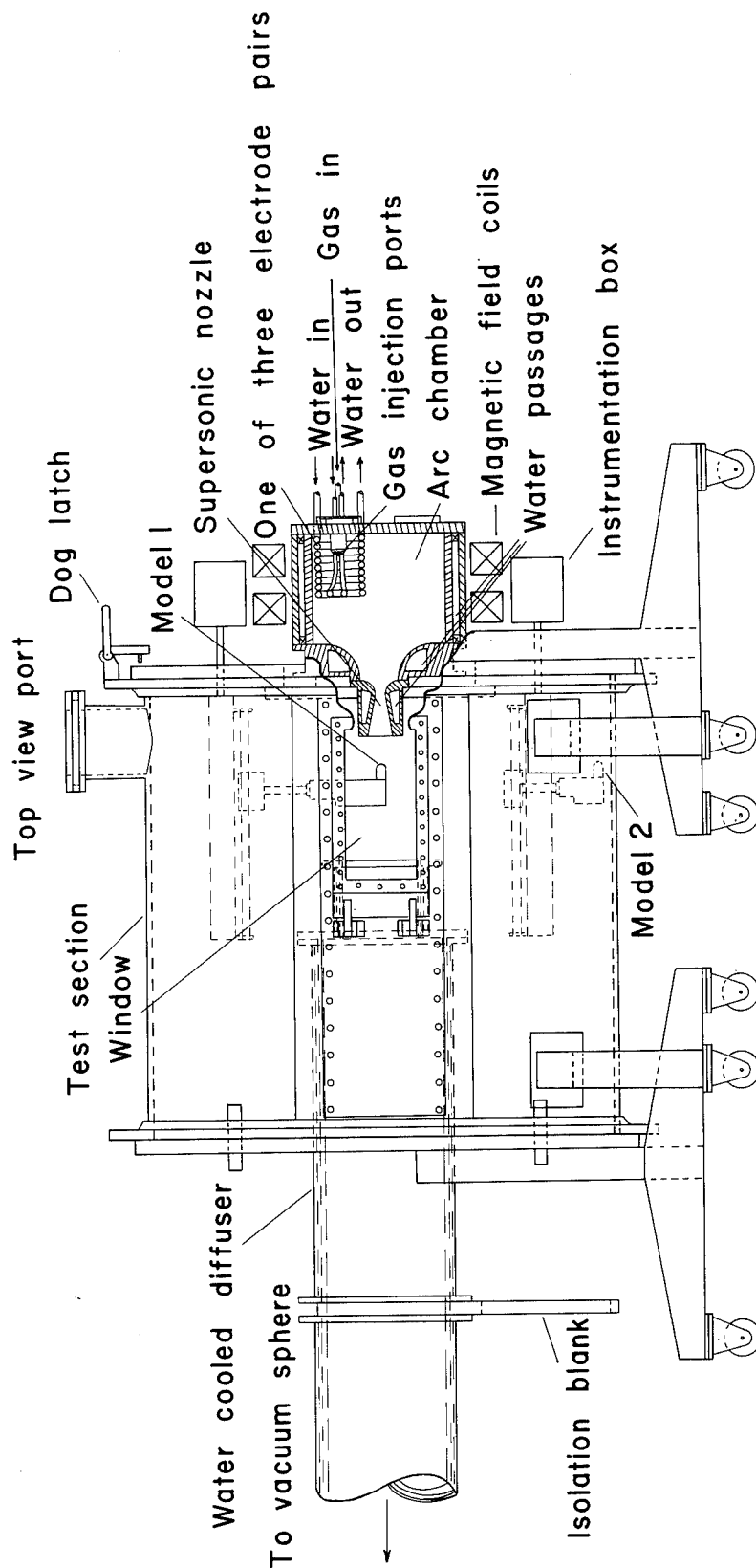
Figure 2.- Ablative model dimensions and thermocouple locations. Linear dimensions are in centimeters (inches).



(b) Aluminum substrate.

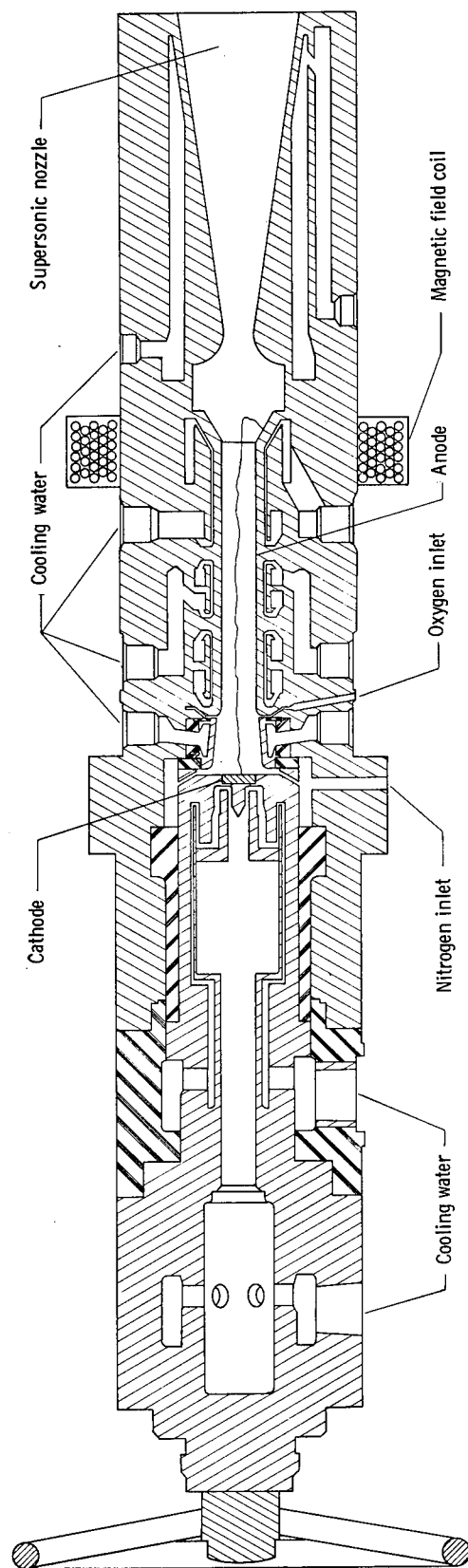
Figure 2.- Concluded.

Thermocouple locations		S/R
Thermo-couples		
1	0	
2	2.14	
3	3.98	
4	6.8	
5	7.65	



(a) Apparatus B arc-heater and test section.

Figure 3.- Test facilities.



(b) Apparatus D arc-heater.

Figure 3.- Concluded.

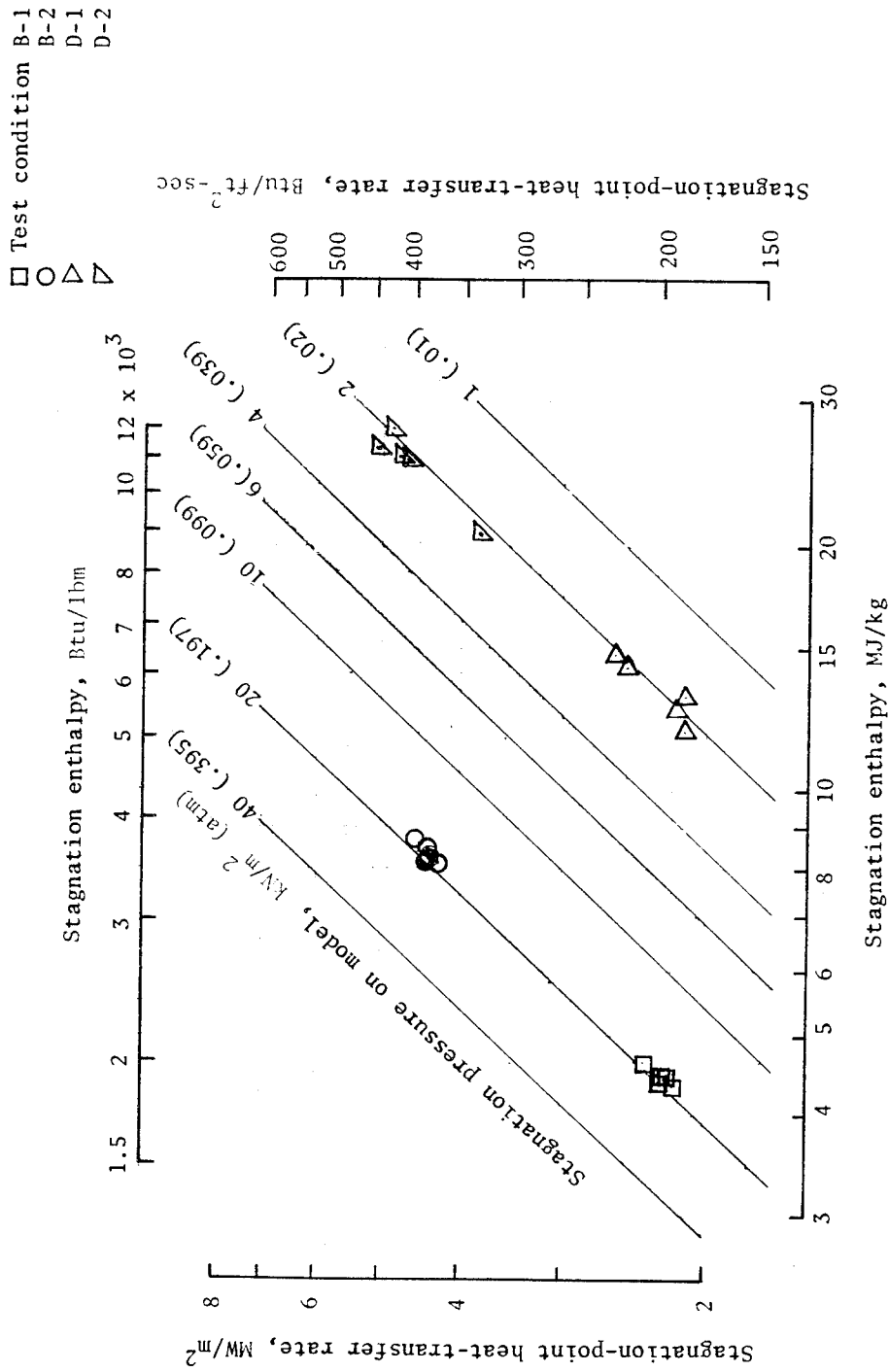


Figure 4.- Stagnation-point test conditions on 0.76-cm-radius (0.3-in.) spherical nose.

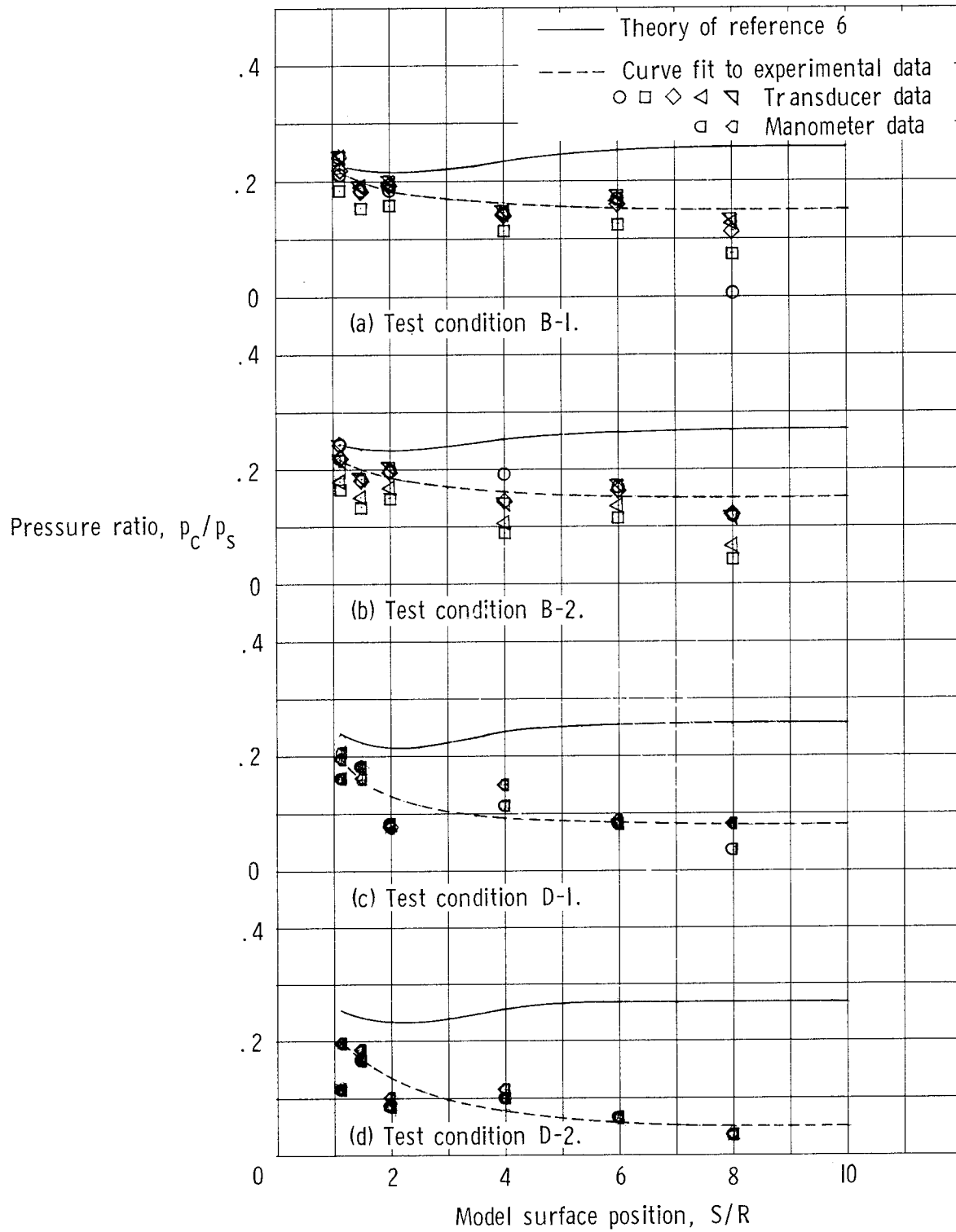


Figure 5.- Pressure distribution on spherically blunted
0.44-radian (25°) half-angle cone.

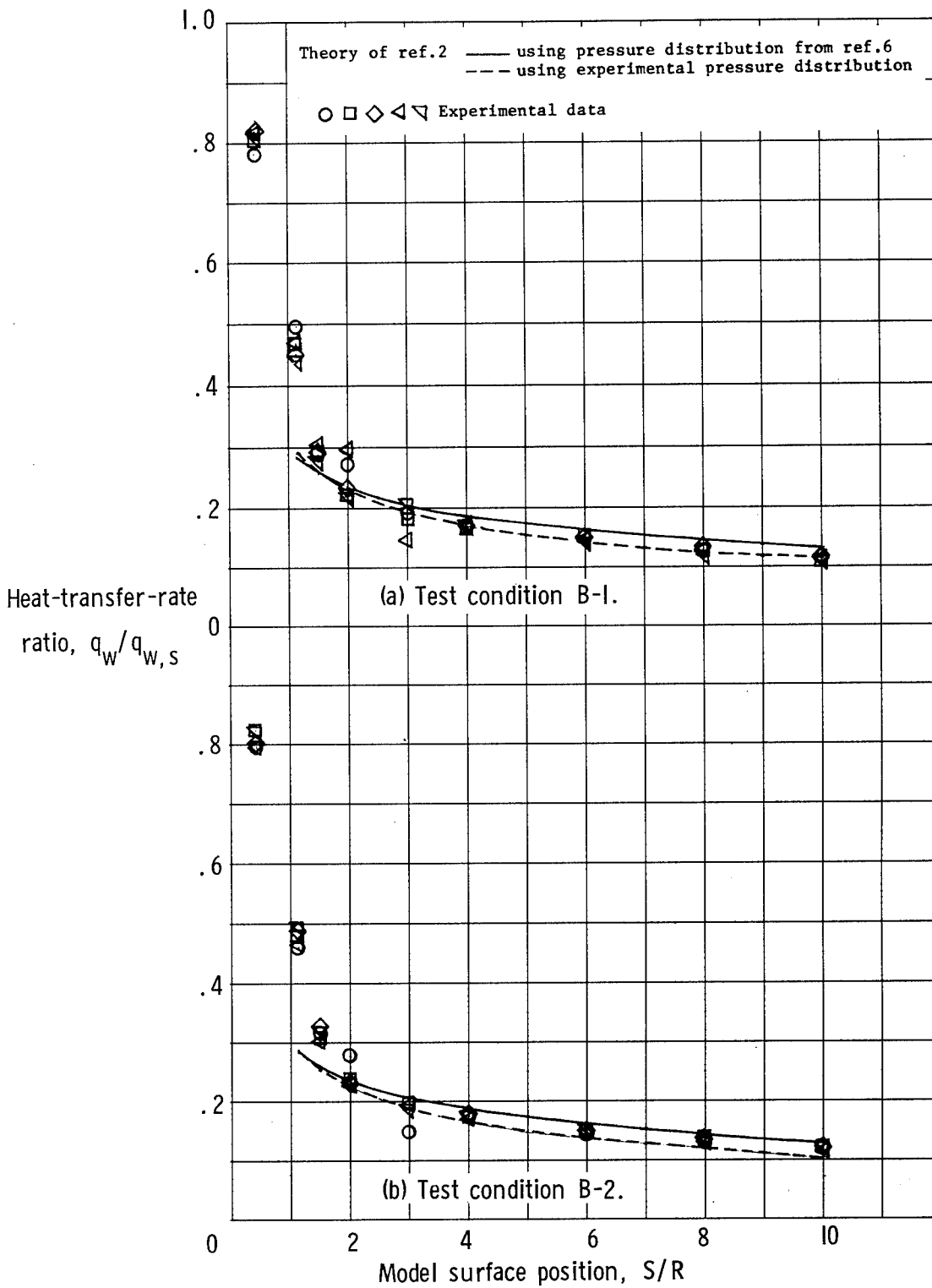


Figure 6.- Heat-transfer-rate distribution on spherically blunted 0.44-radian (25°) half-angle cone.

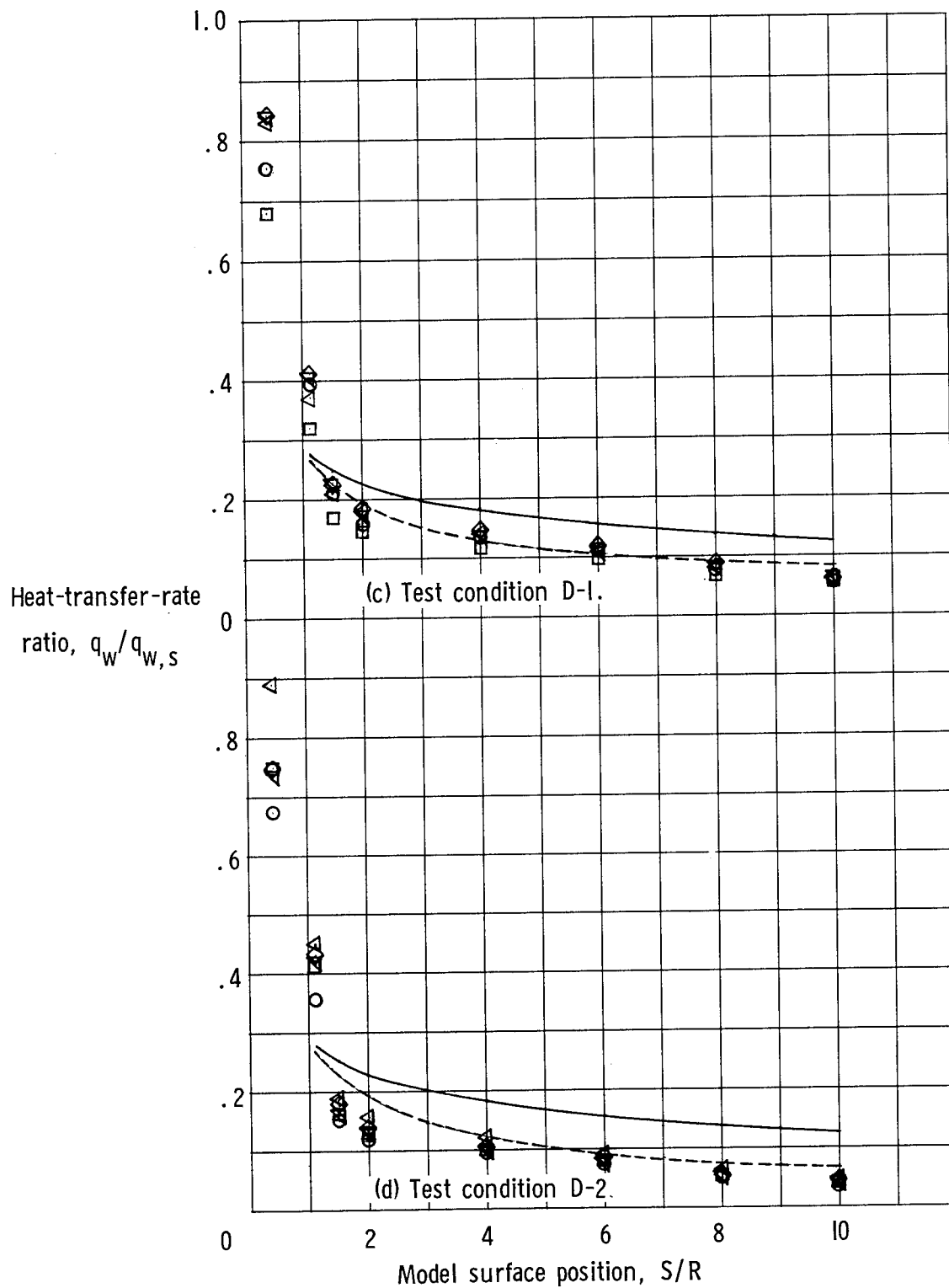
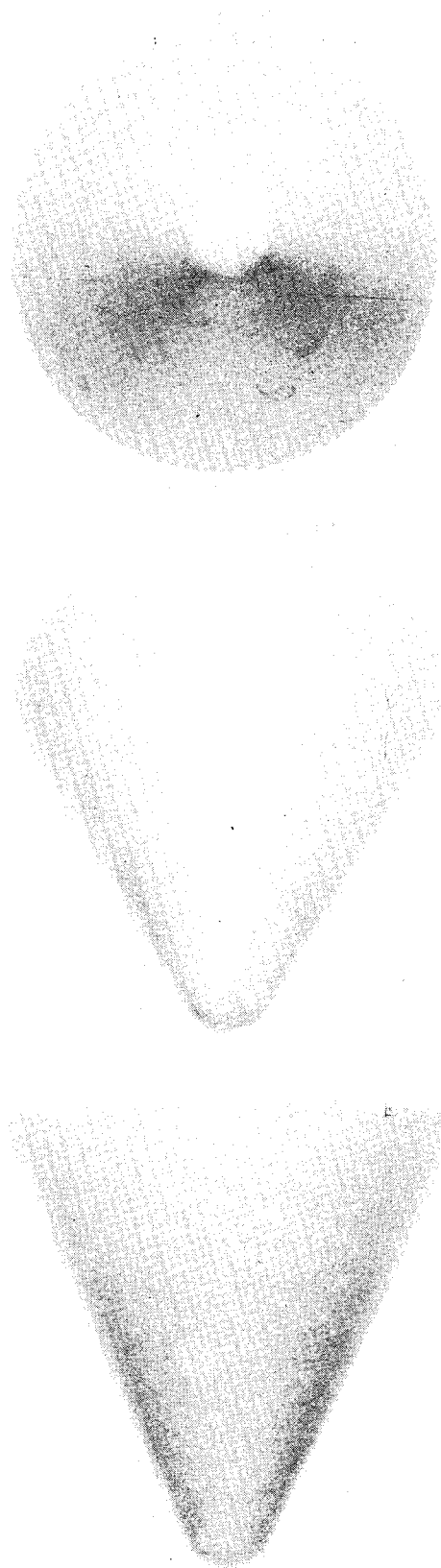
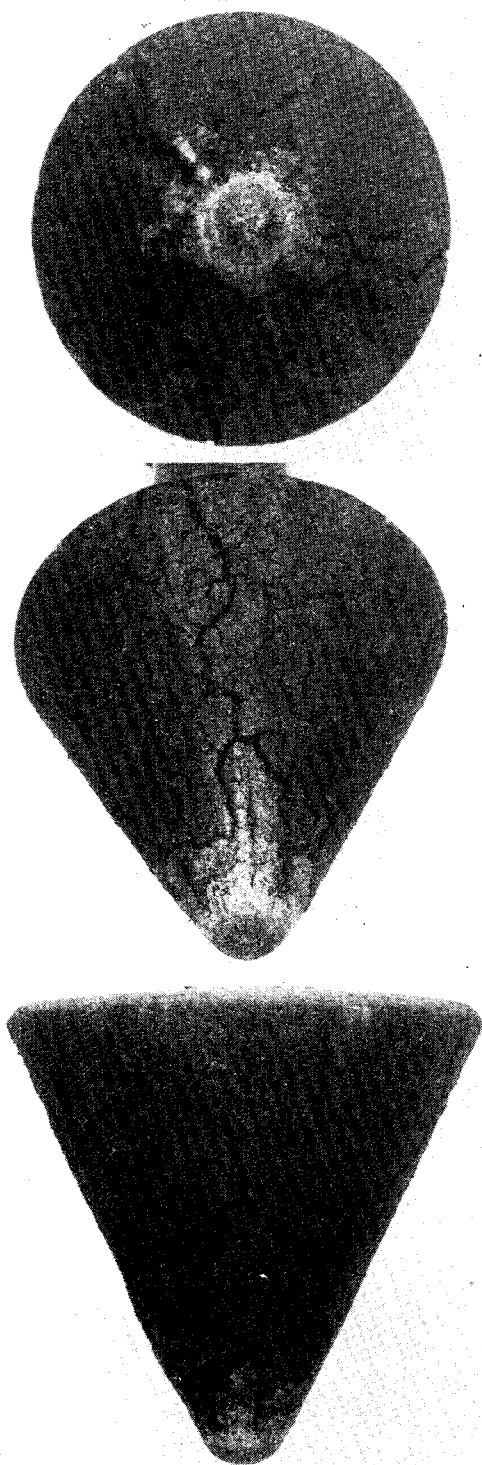


Figure 6.- Concluded.

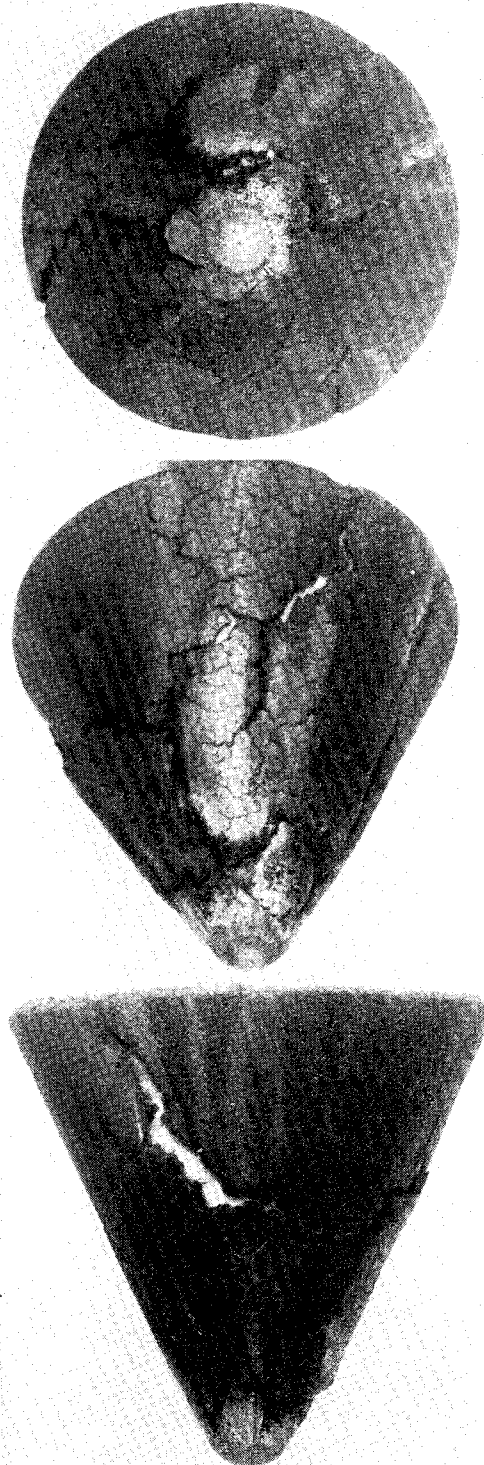


L-72-2487

Figure 7.- Ablative models before test. Material I.



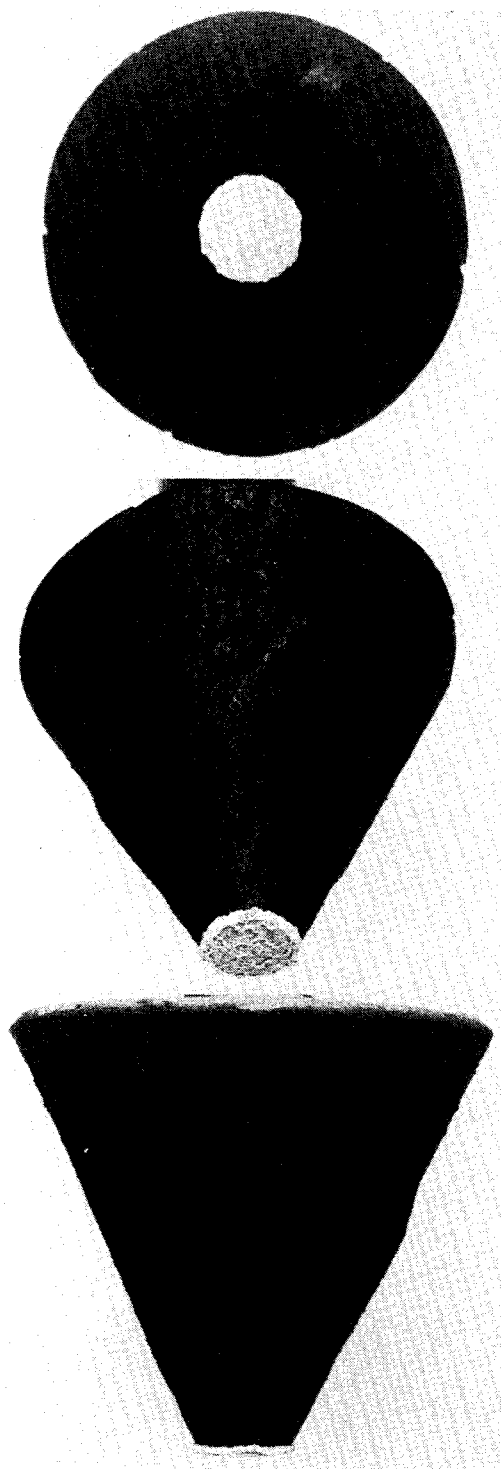
(a) Ablative material I.



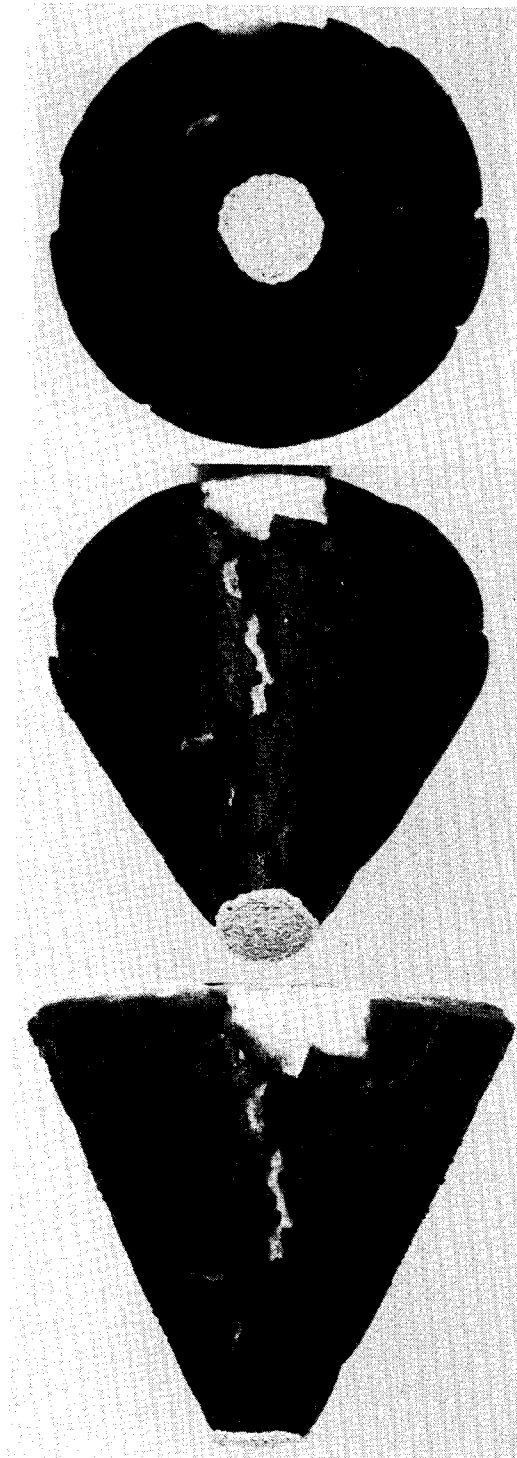
(b) Ablative material II.

L-72-2488

Figure 8.- Models after testing at condition B-1.



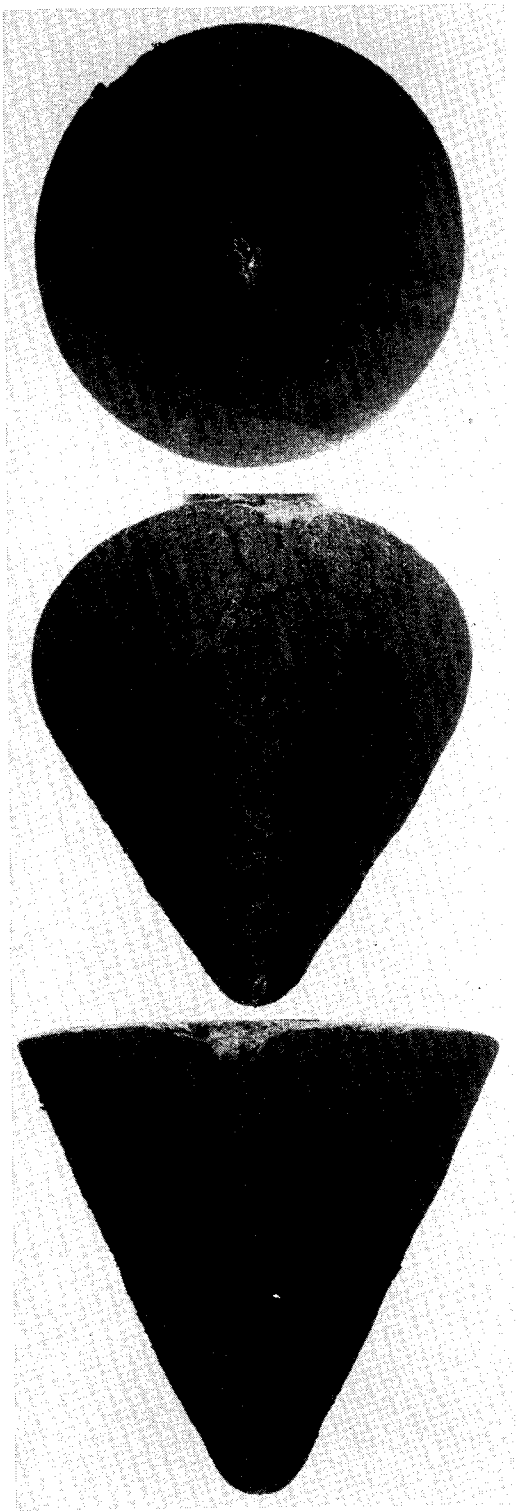
(a) Ablative material I.



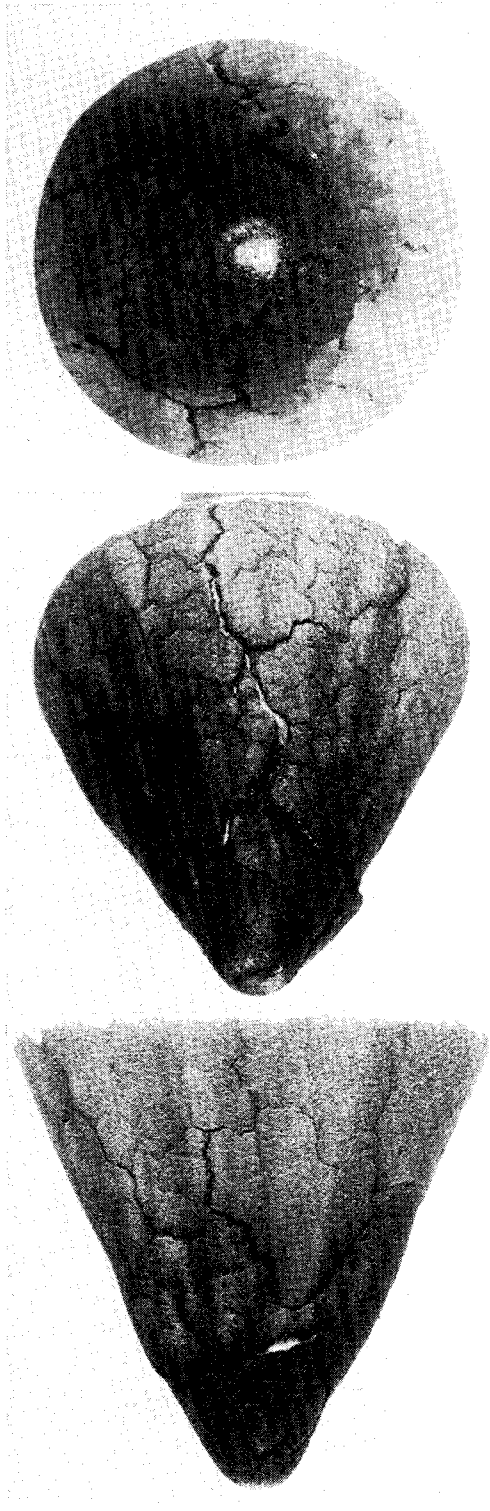
L-72-2489

(b) Ablative material II.

Figure 9.- Models after testing at condition B-2.



(a) Ablative material I.



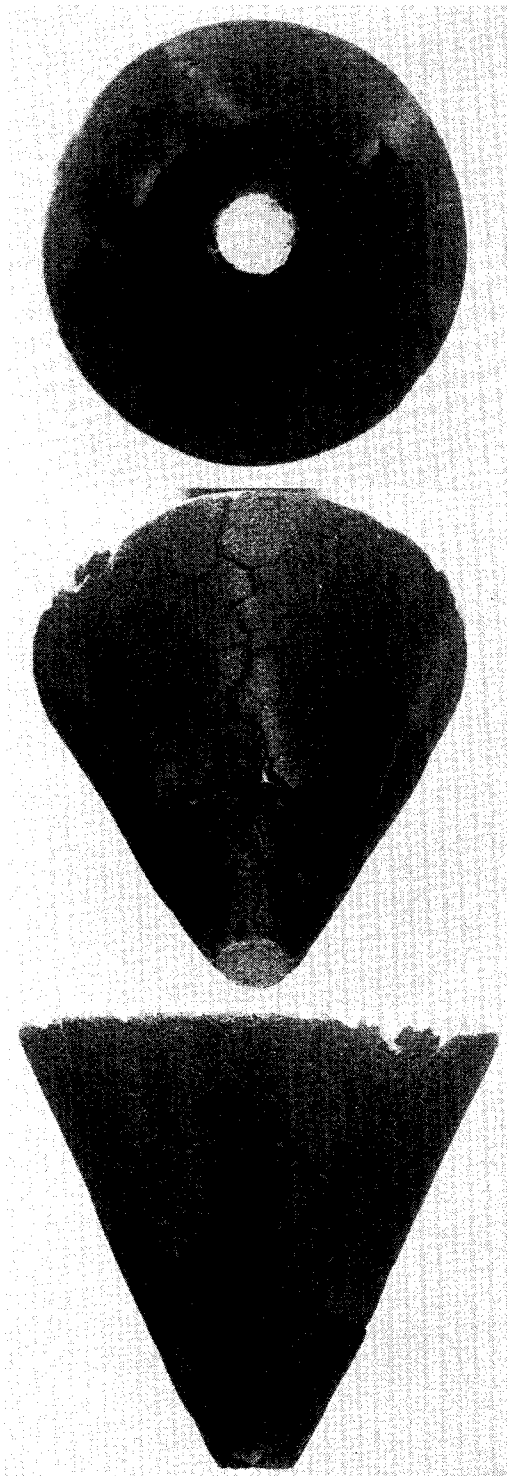
(b) Ablative material II.

L-72-2490

Figure 10.- Models after testing at condition D-1.



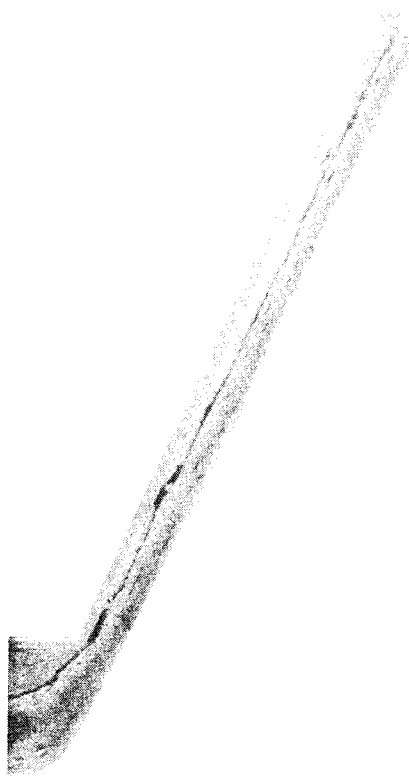
(a) Ablative material I.



(b) Ablative material II.

L-72-2491

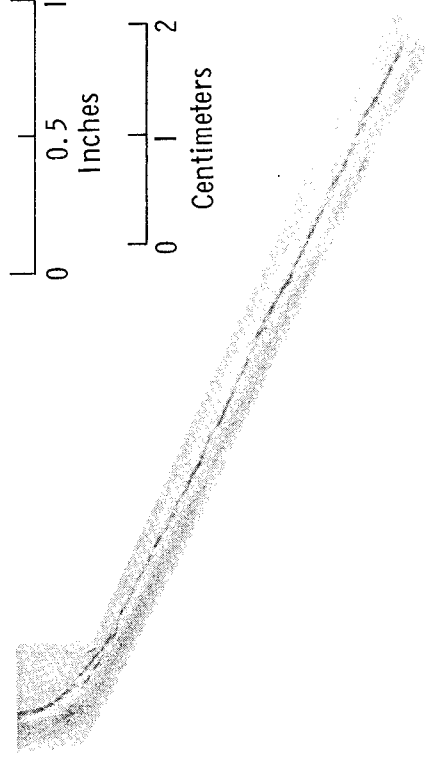
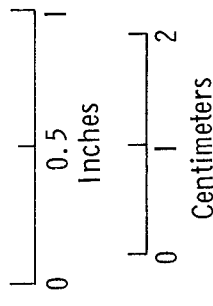
Figure 11.- Models after testing at condition D-2.



(a) Test condition B-1.



(c) Test condition D-1.



(b) Test condition B-2.



(d) Test condition D-2.

L-72-2492

Figure 12.- Sections of models with ablative material I after testing.

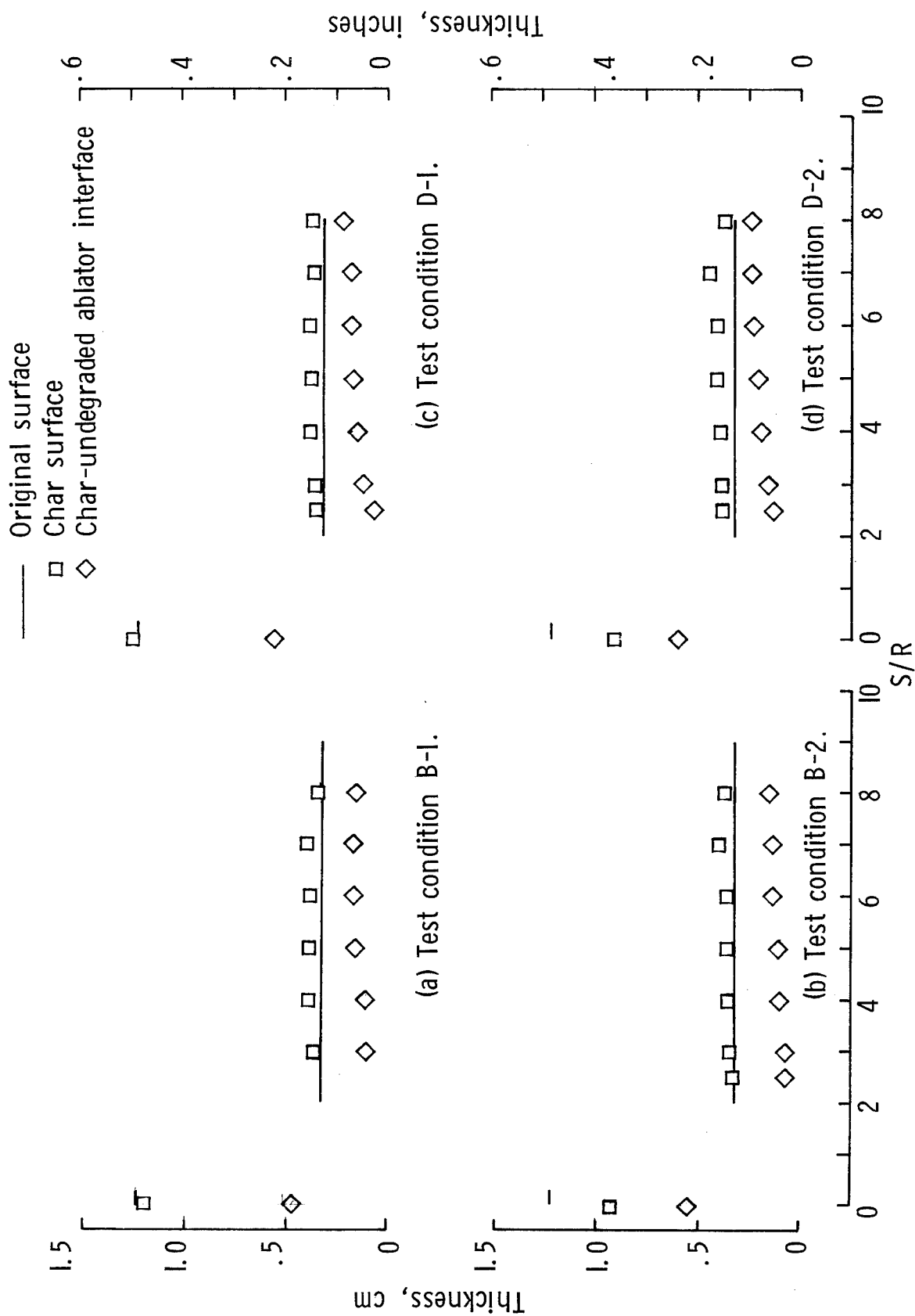
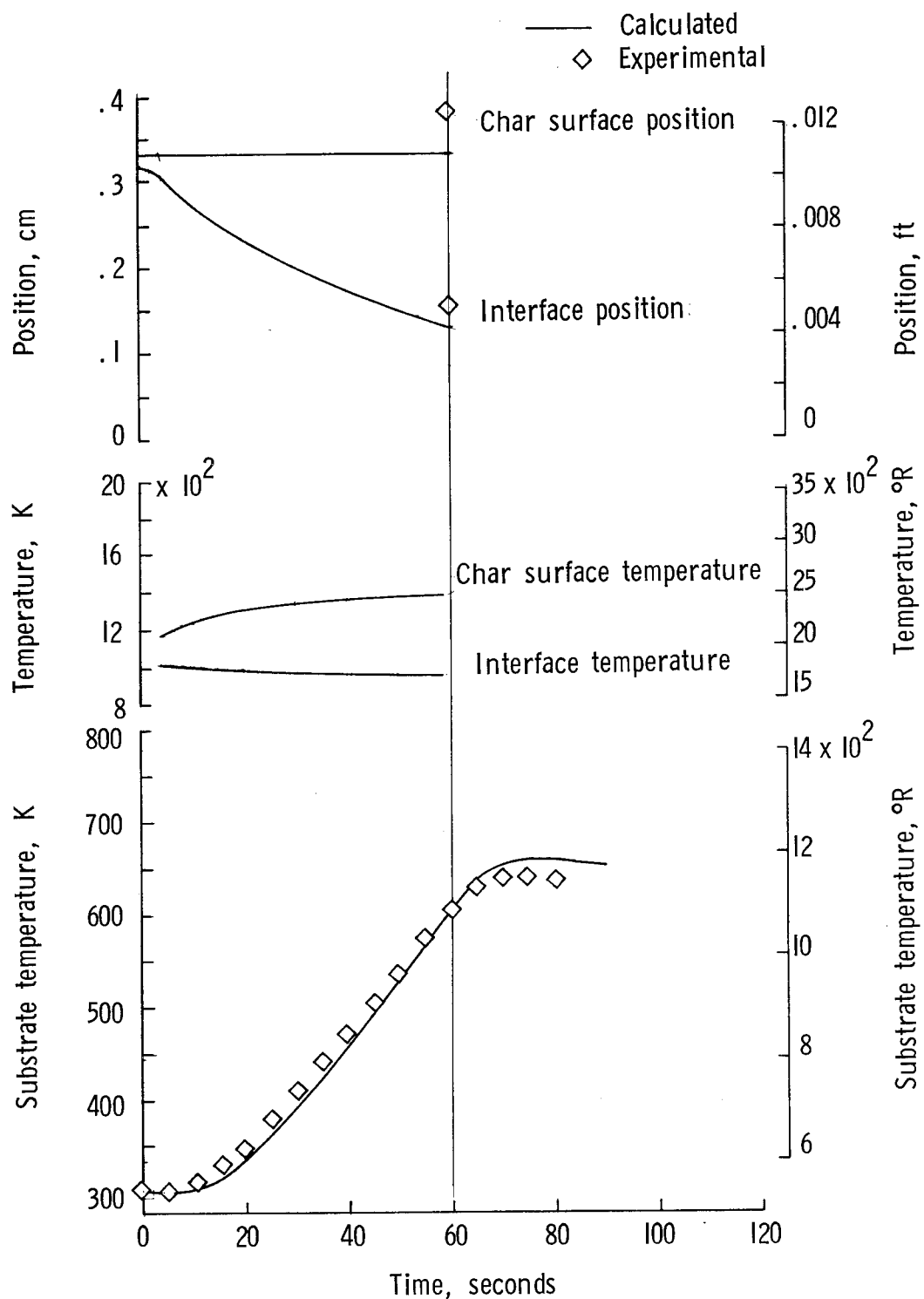
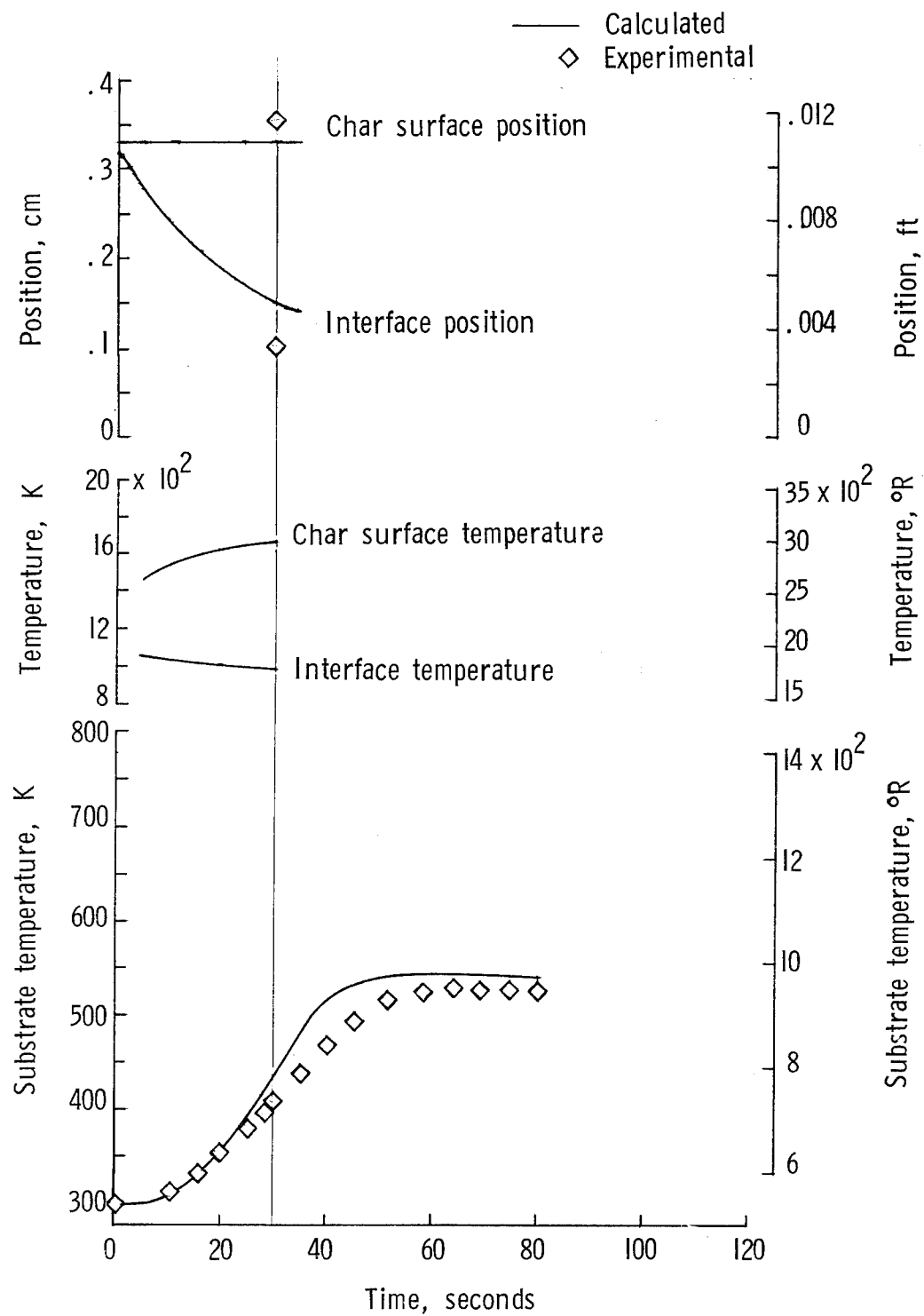


Figure 13.- Char-layer and undegraded-layer thickness. Material I on inconel substrate.



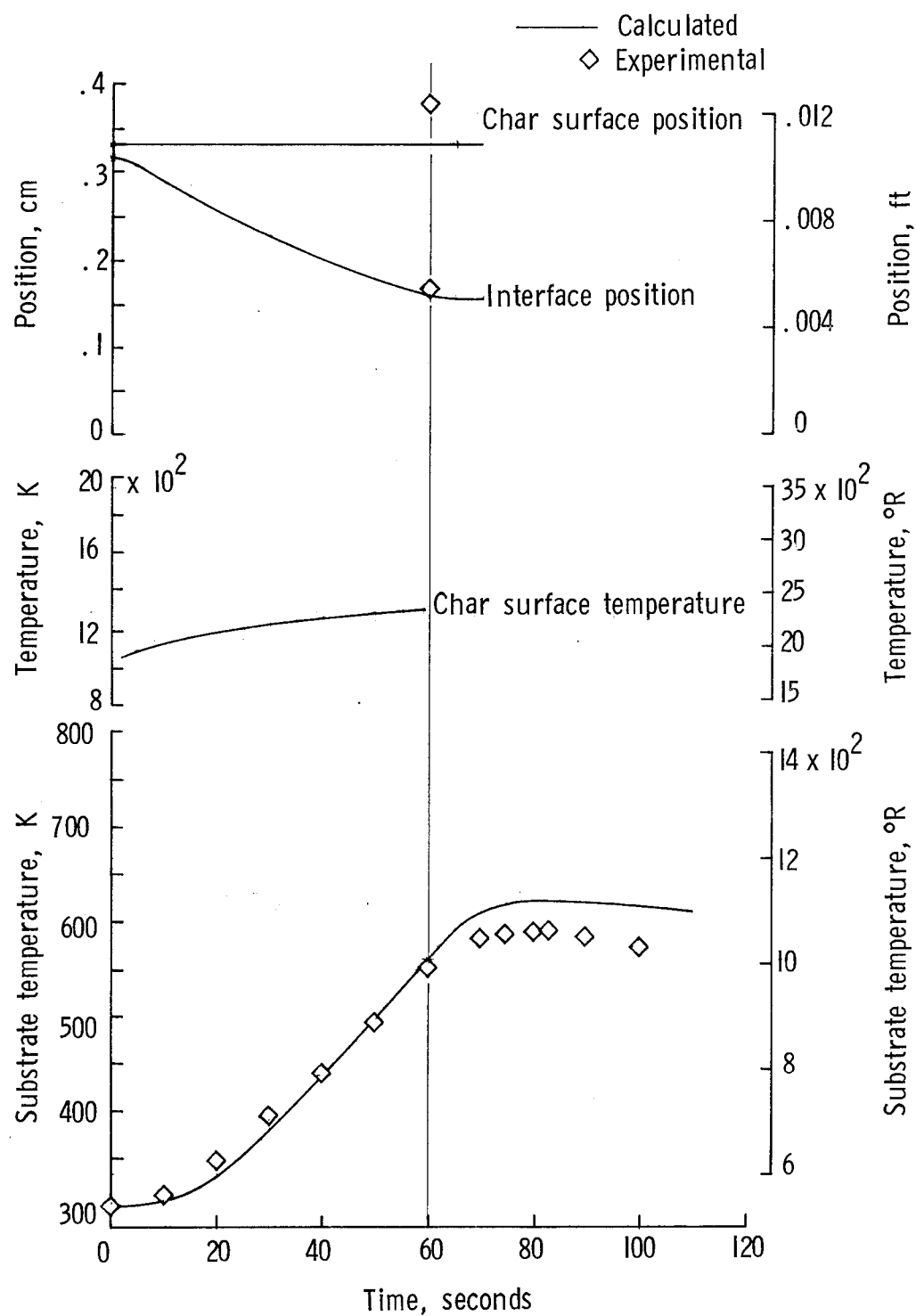
(a) Test condition B-1.

Figure 14.- Experimental and calculated recession and temperatures on afterbody (S/R = 5) of a 0.44-radian (25°) conical ablative model with inconel substrate.



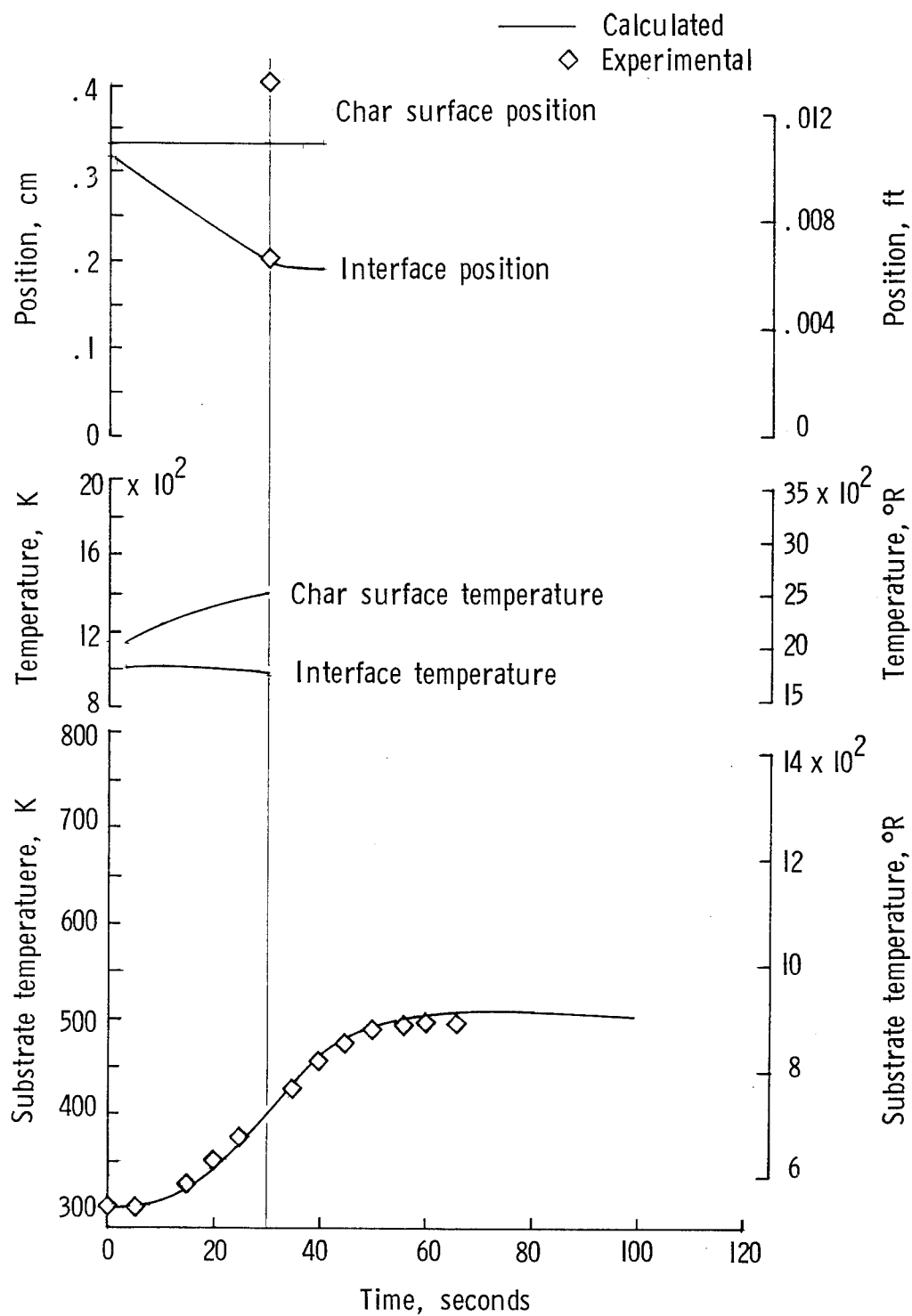
(b) Test condition B-2.

Figure 14.- Continued.



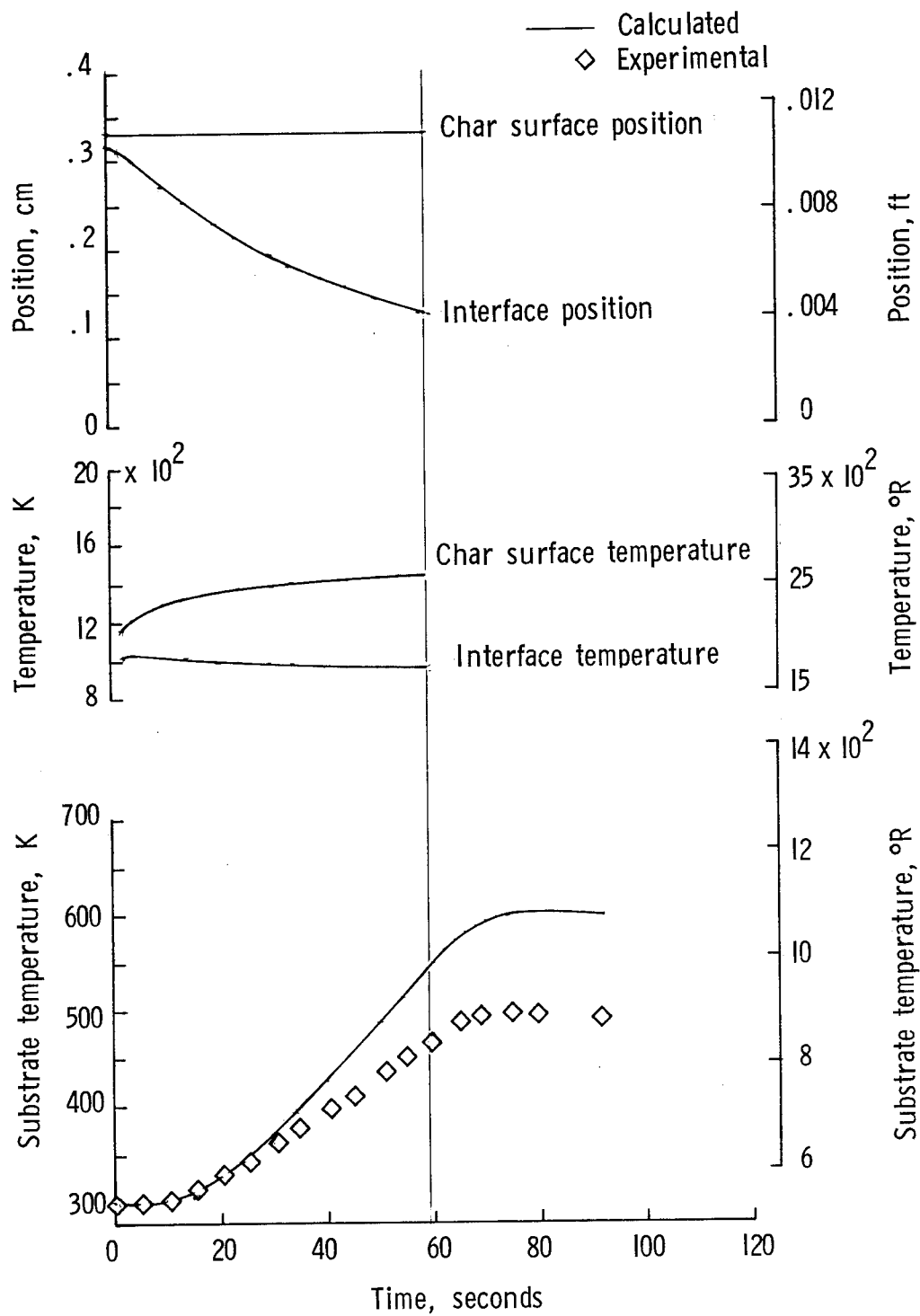
(c) Test condition D-1.

Figure 14.- Continued.



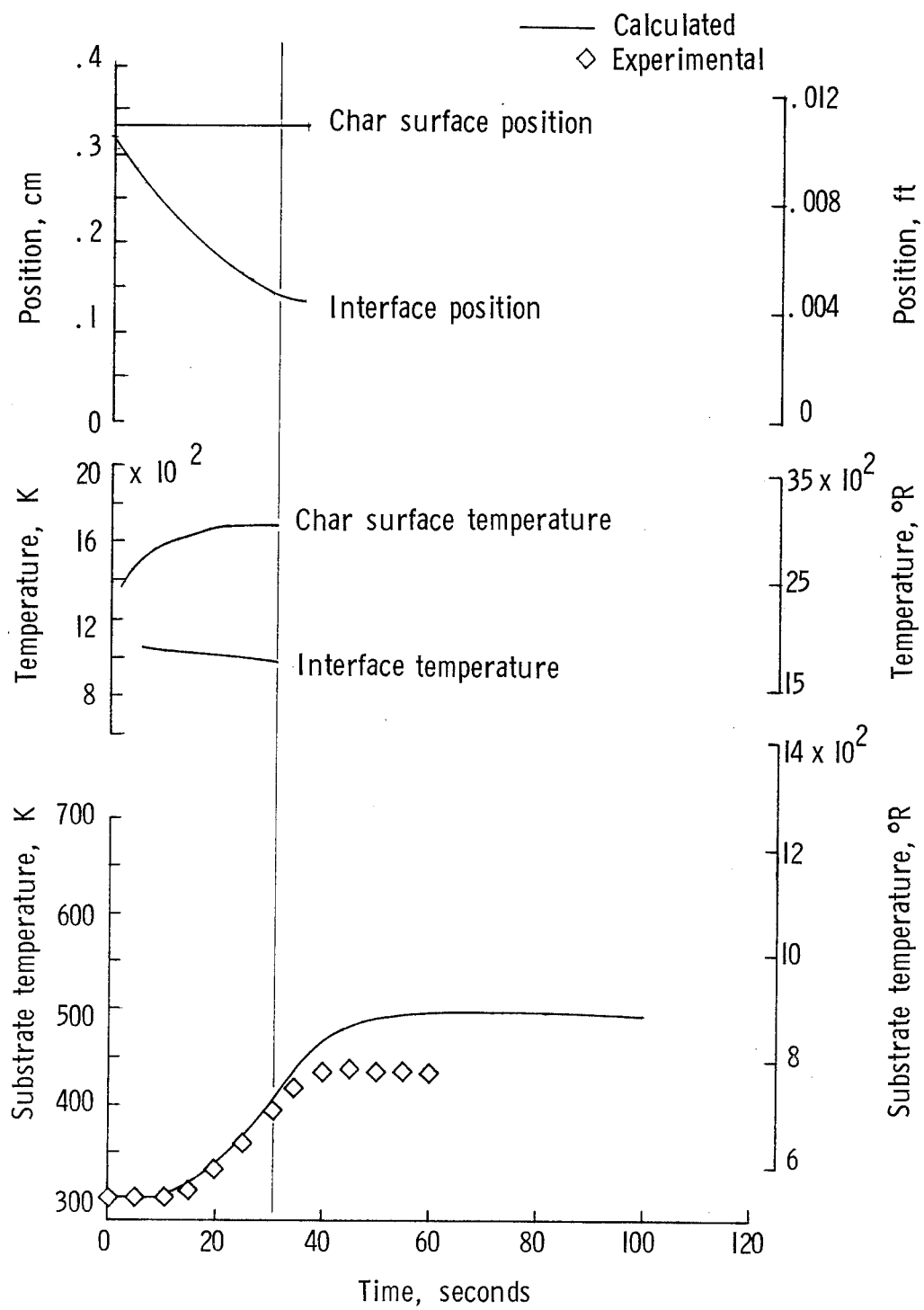
(d) Test condition D-2.

Figure 14.- Concluded.



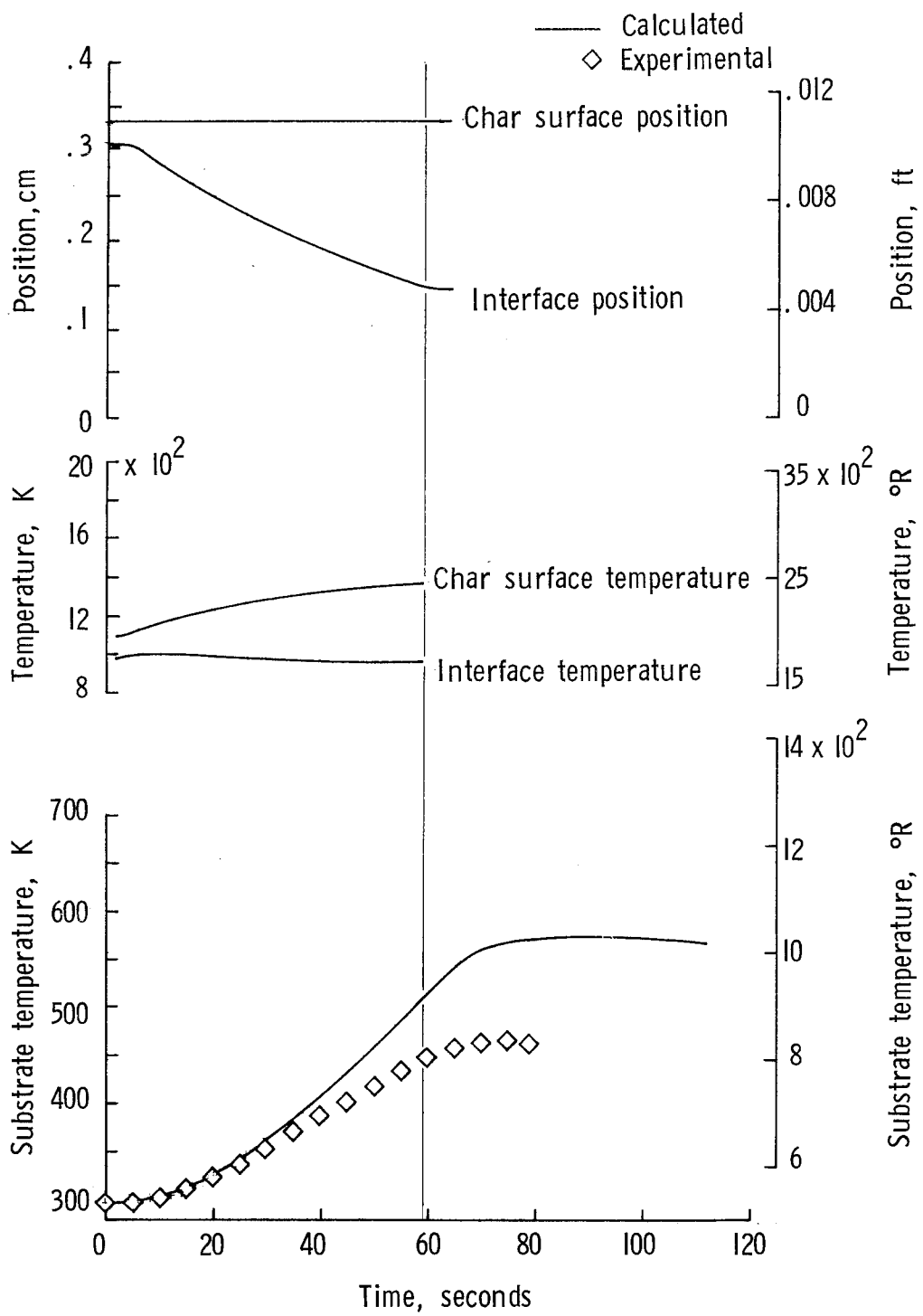
(a) Test condition B-1.

Figure 15.- Experimental and calculated ablator recession and temperatures on afterbody (S/R = 4) of a 0.44-radian (25°) conical ablative model with aluminum substrate.



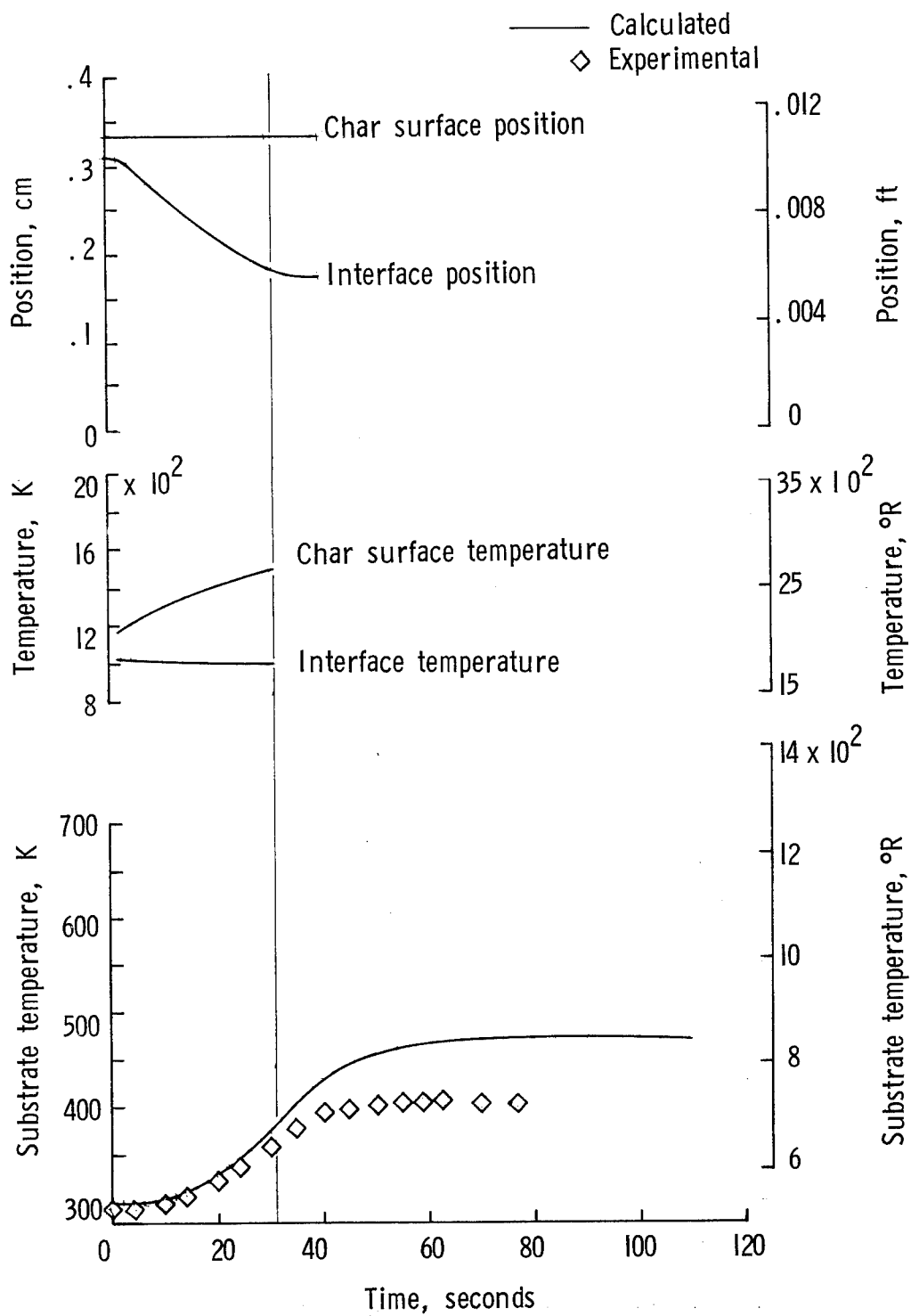
(b) Test condition B-2.

Figure 15.- Continued.



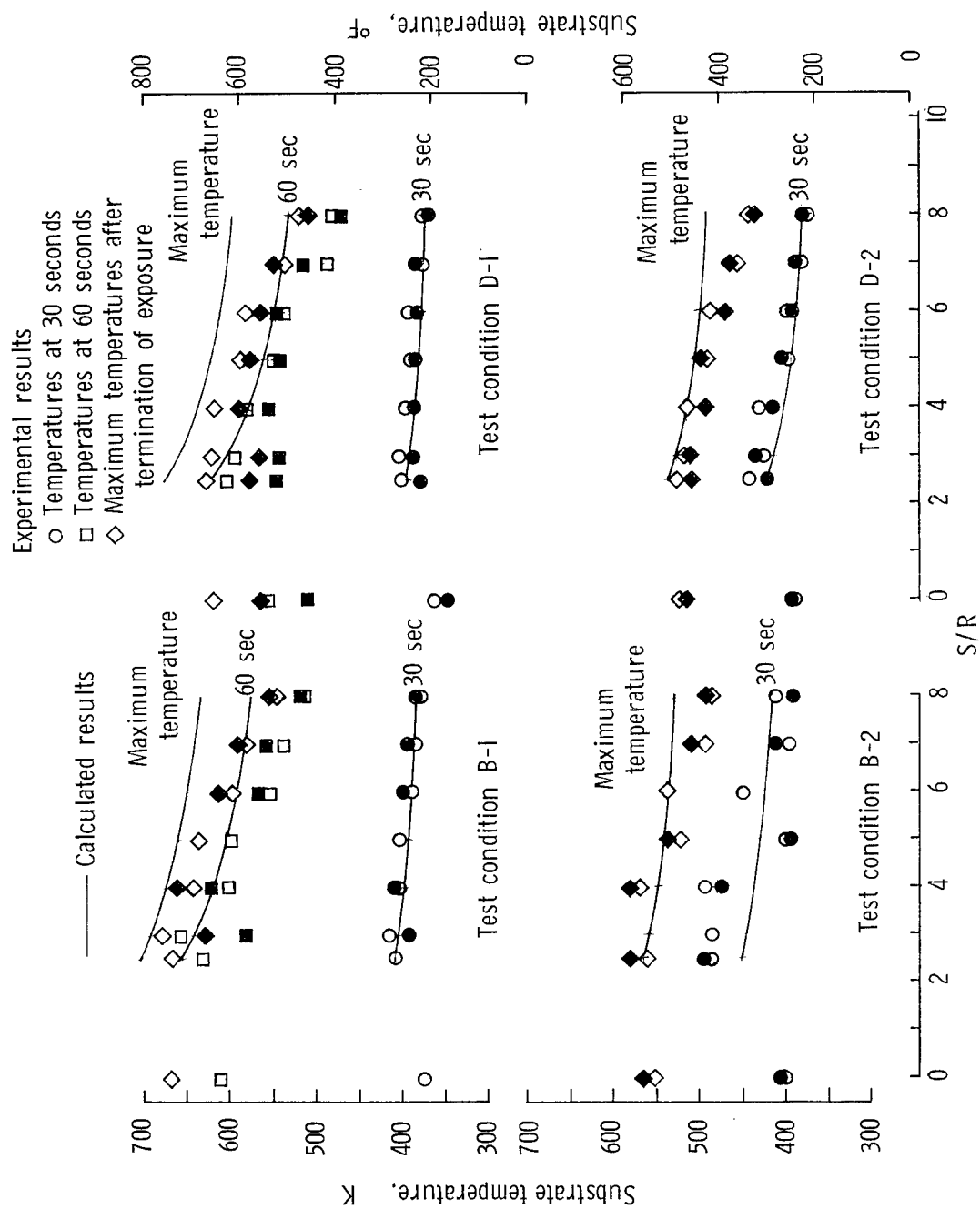
(c) Test condition D-1.

Figure 15.- Continued.



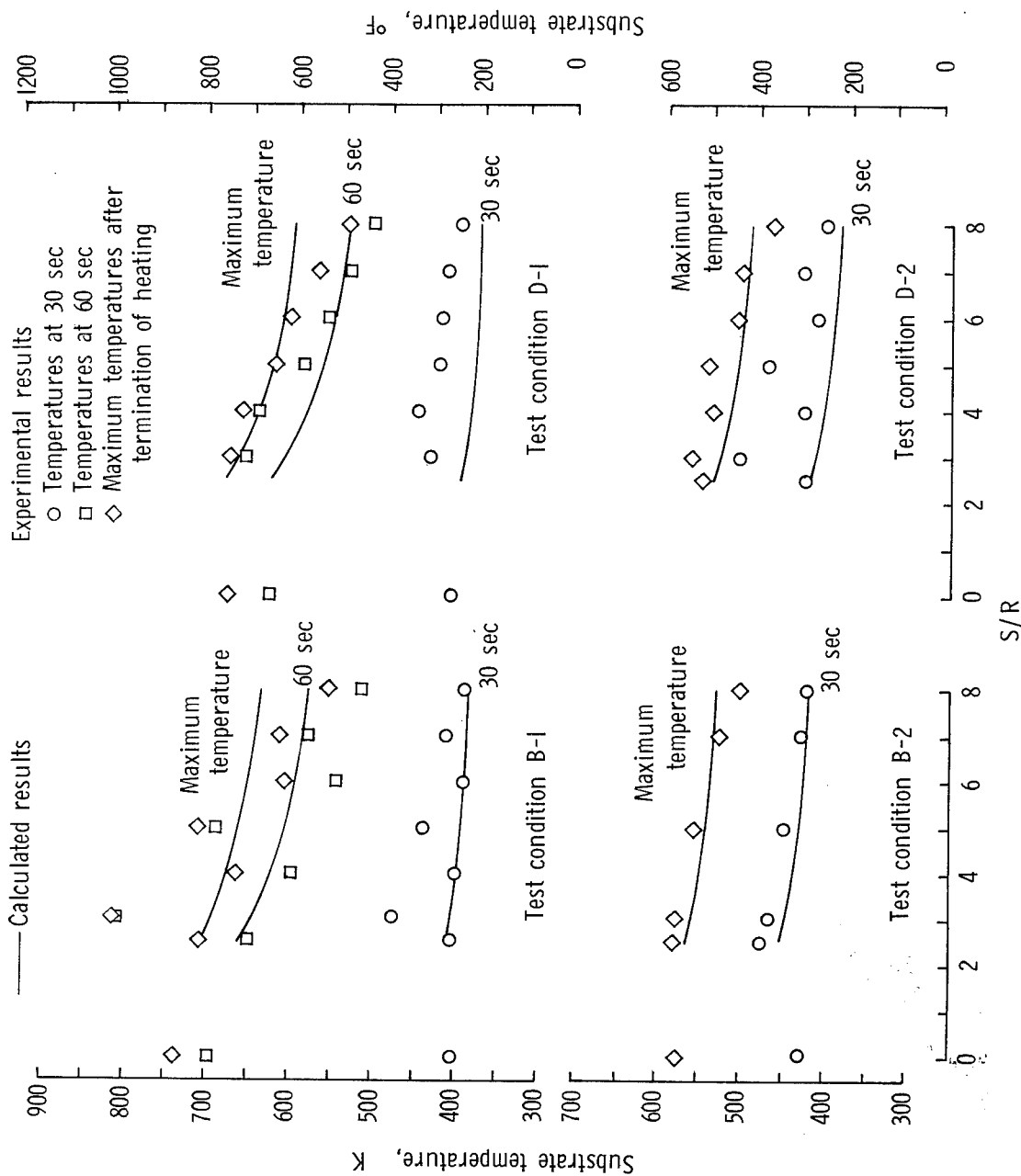
(d) Test condition D-2.

Figure 15.- Concluded.



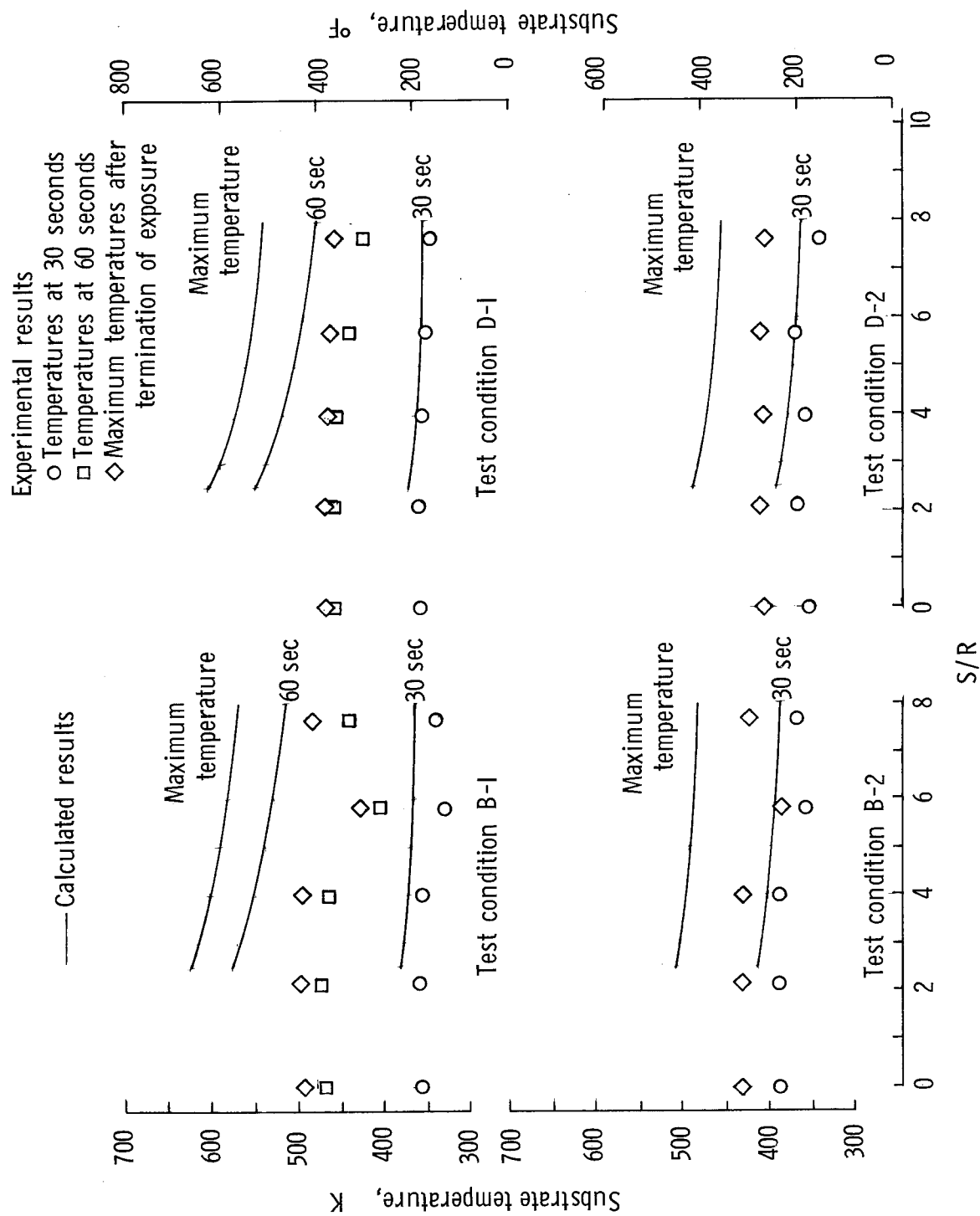
(a) Ablative material I on inconel substrate.

Figure 16.- Substrate temperature distributions on 0.44-radian (25°) conical ablative model. Open and solid symbols indicate different tests.



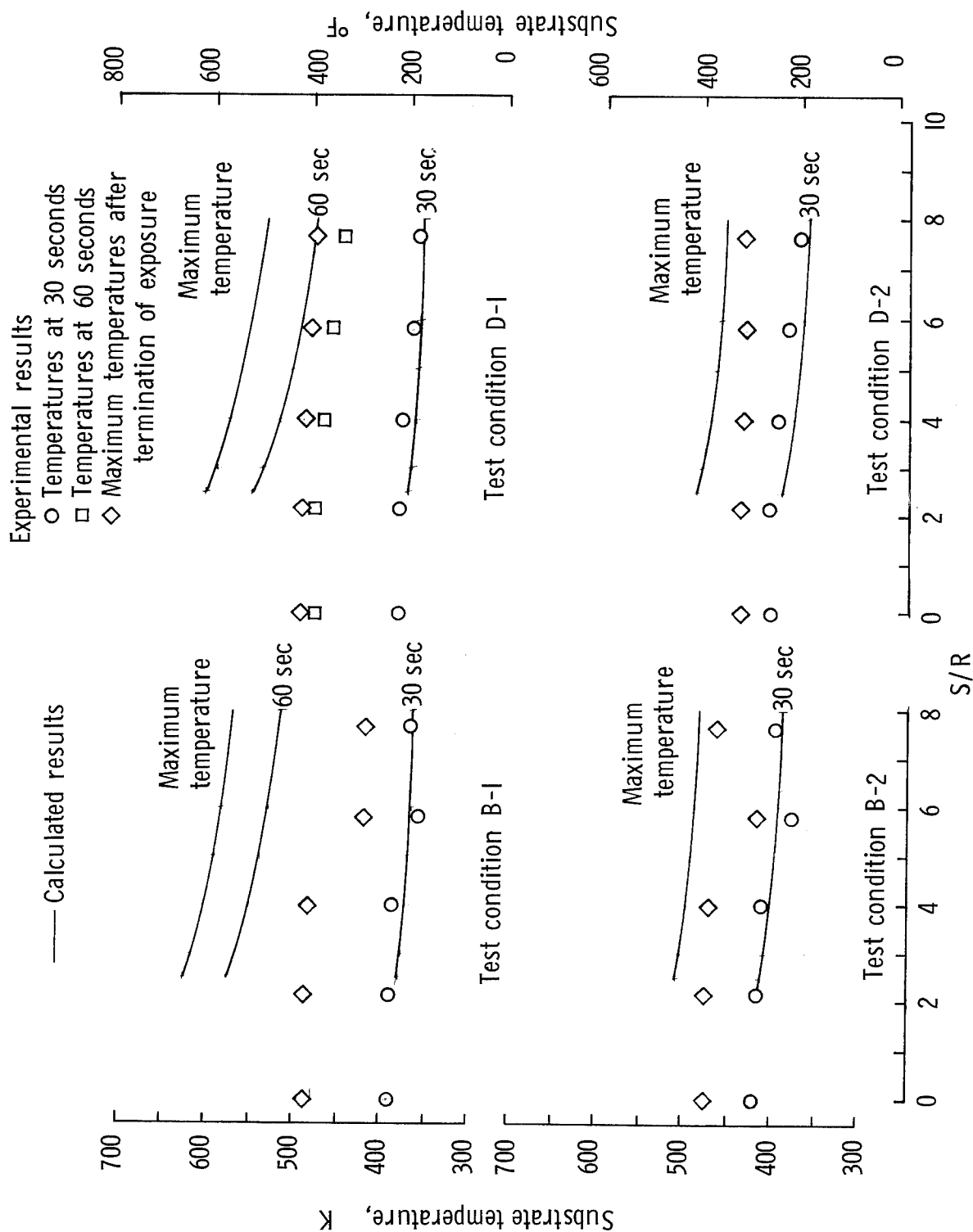
(b) Ablative material II on inconel substrate.

Figure 16.- Continued.



(c) Ablative material I on aluminum substrate.

Figure 16.- Continued.



(d) Ablative material II on aluminum substrate.

Figure 16.- Concluded.